Deutsches Zentrum
für Luft- und Raumfahrt

Fracture analysis on asteroid Ryugu

Master Thesis in Geological Sciences

at

Freie Universität, Institut für Geologische Wissenschaften, Berlin

and

Deutsches Zentrum für Luft- und Raumfahrt
Institut für Planetenforschung, Adlershof

Handed in by:	Leonard Schirner
E-Mail (University):	schirnel00@zedat.fu-berlin.de
E-Mail (private):	leonardschirner@gmail.com / leonard.schirner@dlr.de
Student Number:	5493489
Primary Corrector:	Prof. Dr. Georg Kaufmann
Secondary Corrector:	Dr. Katharina Otto
Supervisor:	Dr. Katharina Otto
Current Semester:	6th MA semester
Date handed in:	July 2023

Erklärung zur Urheberschaft

Ich habe die Arbeit selbständig verfasst, keine anderen als die angegebenen Quellen und Hilfsmittel benutzt, sowie alle Zitate und Übernahmen von fremden Aussagen kenntlich gemacht.

Die Arbeit wurde bisher keiner anderen Prüfungsbehörde vorgelegt. Die vorgelegten Druckexemplare und die vorgelegte digitale Version sind identisch.

Berlin, July 2023

_____

Signature

Contents

List of Figures

List of Tables

Zusammenfassung

In dieser Arbeit wurden Risse in Gesteinsbrocken auf dem erdnahen Asteroiden Ryugu kartiert und analysiert, wofür Bilddaten der japanischen Hayabusa-2-Mission verwendet wurden.

Daraus abgeleitet wurden Orientierungsverteilungen und Längenverteilungen der Risse. Die bevorzugte Ausrichtung der Risse ist Nord-Süd bezogen auf Ryugus Äquator. Die wahrscheinliche Erklärung für diese Verteilung ist der thermische Einfluss, durch den diese Risse entstanden sind: Die Sonne beleuchtet am Morgen die Ostseite der Felsbrocken und am Abend die Westseite. Dies führt zu einem thermischen Gradienten in Ost-West-Richtung, der wiederum eine Spannungsverteilung verursacht, die das Risswachstum in Nord-Süd-Richtung begünstigt.

Die für Ryugu ermittelte Verteilung der Risslängen ähnelt den Rissen auf einem anderen Asteroiden, Bennu, der ebenfalls auf einer erdnahen Bahn kreist.

Die Längenverteilung lässt sich erklären, indem der thermale Einfluss durch ein Exponentialgesetz beschrieben wird und die Größe der Gesteinsbrocken (und damit auch der Risse) durch ein Potenzgesetz.

Die Längenverteilung wurde auch für die Modellierung der zeitlichen Abfolge des Risswachstums verwendet um Zeitskalen zu erhalten, in denen das Risswachstum stattfand und die beobachteten Längenverteilungen entstanden sein könnten.

Abstract

Fractures in boulders on the Near-Earth-Asteroid Ryugu were mapped and analysed in this work, using image data from the Japanese Hayabusa-2 mission.

This resulted in orientation distributions and length distribution of the fractures. The preferred orientation of the fractures is North-South, relative to Ryugu's equator. The likely explanation for this distribution is the thermal influence under which these fractures formed: The sun illuminates the east side of the boulders in the morning and the west side in the evening, resulting in a thermal gradient in the east-west direction, the thermal gradient in a stress distribution that promotes crack

growth in the north-south direction.

The distribution of fracture lengths determined for Ryugu is similar to the fractures on another asteroid, Bennu, which also orbits in a near-Earth orbit.

The length distribution can be explained by describing the thermal influence with an exponential law and the size of the boulders (and thus also the fractures) with a power law.

The length distribution was also used to model the temporal sequence of fracture growth to obtain time scales when fracture growth occurred and the observed length distributions could have formed.

1. Motivation

How did our world form? Why is there life on Earth? Why is there water on Earth? Could humanity prevent and survive a extinction event that killed the dinosaurs? Are there enough resources for humanity's future?

A step towards answering these questions might come from research on asteroids and other small bodies, as they are the remnants of the early solar system and witnesses of the epoch of planet formation, about 4 billion years ago. Asteroid impacts can be one of the biggest threats humanity could face, but they could potentially also be what makes humanity prosper in the coming centuries via harvesting their metallic resources.

To understand these enigmatic bodies, their foreign environment needs to be researched and the processes that form and shape their surface need to be analyzed. Part of this research is the formation of fractures on asteroid surfaces. Fractures are a well known surface feature, indicative of erosive surface processes that help us understand how small asteroids evolve. By studying fractures on Ryugu, a small near-Earth asteroid about 900 m in diameter, researchers can gain a deeper understanding of the processes that lead to fracture formation, their relationship to the asteroid's geological history, and the implications for the behavior of asteroids as a whole. Furthermore they teach us how the information from their surfaces correlate with their original pristine nature.

To investigate the fracture origin, fractures on the rubble-pile asteroid Ryugu are mapped and analysed in this thesis. Ryugu possesses several unique characteristics and properties that make it an ideal target for investigating fractures and their implications: The Japanese mission, Hayabusa2, successfully visited Ryugu and collected a wealth of image data using state-of-the-art instruments. The mission provided high-resolution images and detailed surface topography, enabling a thorough anal-

ysis of fractures on Ryugu's surface and their characteristics. Ryugu is classified as a rubble-pile asteroid, which means it is composed of numerous rocky fragments loosely held together by gravitational forces. This structure is of particular interest because it can affect how fractures propagate and evolve on the asteroid's surface. Furthermore Ryugu is a primitive, carbon-rich asteroid that has preserved material from the early solar system. By studying fractures on Ryugu, scientists can gain insights into the processes that occurred during the formation and evolution of asteroids, providing valuable information about the origins of our solar system. Ryugu also exhibits surface features such as craters and regolith. These features suggest past geological activity, potentially including impact events and internal processes. The investigation of fractures on Ryugu's surface can shed light on the mechanisms and dynamics that have shaped its surface over time. These unique characteristics of Ryugu make it an intriguing target for investigating fractures and contribute to our broader understanding of the formation and evolution of asteroids in the solar system.

2. Introduction

2.1. Asteroids

The term "small bodies" generally describes any celestial body smaller than a dwarf planet (about 1000 km in diameter). Any small body, that is not a comet[1], a natural satellite or moon[2] is an asteroid. Asteroids range in size from just a few metres to several hundreds of kilometres. Most asteroids are found between Mars' and Jupiter's orbits, about 2 to 4 astronomical units (AU)[3] away from the sun, giving rise to the term asteroid belt. Since the largest object in the asteroid belt, Ceres, was classified as a dwarf planet in 2008, Pallas is the largest asteroid at 546 kilometres diameter. A comparison of different asteroids to scale is shown in Fig. 1.

Asteroids are typically classified according to their density and chemical composition into 3 main categories: metallic M-types, sillicaceous, stony S-types and carbonaceous C-types. C-type compositions are often called 'primitive' because they are believed to have undergone little changes in the past 4.5 billion years and present the primordial material well, out of which the planets have formed. Since asteroids have no protecting atmosphere, they are subject to the harsh space environment. This includes total vacuum, impactor bombardment of all sizes, high-energy irradiation and extreme temperature variations, with very little gravitational pull; making asteroids a very exotic place in space and therefore highly interesting to study.

Asteroids are the left-over debris from the processes that formed the inner planets. Studying them tells us a lot about the early solar system formation. This could help us explain how water and the building blocks of life came to Earth, potentially

[1] A comet is a celestial object containing ice that undergoes gas emission as it approaches the Sun.
[2] If a celestial body does not orbit around the sun, but instead another body, it is a moon or natural satellite.
[3] An astronomical unit (AU) is the average distance from Earth to the Sun, so about 150 million kilometres.

helping to solve one of the most fundamental mysteries of our planet's origins.

Although most asteroids are located on orbits in the asteroid belt, some of them can deviate from their original asteroid belt orbits due to collisions or orbital resonances. This can and has led to them colliding with planets including Earth. In fact, an asteroid impact is thought to be the cause of the Cretaceous-Paleogene extinction event[4]. Recently the NASA DART mission intentionally collided a spacecraft with an asteroid's moon to test the possibility of altering an asteroids orbit. In case of a potential large impact likely happening with our Earth, this would be the only hope of preventing a catastrophe. These asteroids are called near-earth asteroids and since their orbits are closer to Earths' orbit they are comparatively easier to reach, which is part of the reason why the near-earth asteroids Bennu and Ryugu were selected for their respective missions.

But asteroids could also be beneficial to humanity, the prospect of potentially mining the mineral content of them for use on Earth and in space is gaining more attention. Some asteroids contain high amounts of valuable metals like platinum, gold and iron, as well as rare-earth elements that are essential for modern technology (Andrews et al., 2015). Mining these resources could reduce the reliance on Earth's finite resources and provide materials for future space exploration and colonization. The idea of mining asteroids is still in its infancy, but companies like Planetary Resources and Deep Space Industries have already been founded with the goal of making it a reality. However, there are also concerns about the environmental impact and ethical considerations of asteroid mining, as well as the potential for conflicts over ownership and extraction rights. Despite these challenges, the study and exploration of asteroids remain an important area of research and discovery in the field of space exploration.

2.2. Rubble-pile asteroids

Rubble-pile asteroids are a type of asteroid characterized by their loosely-bound, agglomerated structure composed of various-sized rocks, boulders, and dust held

[4]The K-T extinction event, about 66 million years ago, is responsible for the extinction of the dinosaurs.

Asteroid	Mission	Year
951 Gaspra	Gallileo	1991
243 Ida	Gallileo	1993
253 Mathilde	NEAR Shoemaker	1997
433 Eros	NEAR Shoemaker	1998
9969 Braille	Deep Space 1	1999
5535 Annefrank	Stardust	2002
25143 Itokawa	Hayabusa	2005
2867 Steins	Rosetta	2008
21 Lutetia	Rosetta	2010
4 Vesta	Dawn	2011
4179 Toutatis	Chang'e2	2012
162173 Ryugu	Hayabusa2	2018
101955 Bennu	OSIRIS-REx	2018

Table 1.: Asteroids visited by spacecrafts

together by their own gravity (Walsh, 2018). These asteroids are thought to have formed as a result of collisions between larger parent bodies, which shattered into fragments that eventually reassembled into a new object (Michel et al., 2001).

The surface of a rubble-pile asteroid can be highly irregular, with varying density and porosity (Bottke et al., 2005). These asteroids are believed to be a common type of small bodies in the solar system, and are considered to be potential threats to Earth if they were to impact our planet. As other asteroids, rubble-pile asteroid often contain rounded grains, called chondrules, they are thought to be molten droplets, that solidified in space (Johansen et al., 2015).

In recent years, several spacecraft missions, including NASA's OSIRIS-REx (Lauretta et al., 2017) and Japan's Hayabusa2 (S. Watanabe et al. (2019)), have visited and sampled rubble-pile asteroids, providing important data for scientific investigations.

2.3. Ryugu

Ryugu is a near-earth rubble-pile asteroid with a diameter of about 900 metres and boulders in the range of 1 to 139 metres. See (Wada et al., 2018) and (Michikami et al., 2019) as well as Fig. 2 and Fig. 4. Its surface has a high abundance of boulders in a wide range of sizes, see Fig. 5. The cumulative size distribution of Ryugus

Boulders follows a power law with an exponent of -2.65 according to Michikami et al. (2019). The boulders have been classified earlier in three major categories, with a correlation between brightness and morphology: Dark and rugged boulders, bright and smooth boulders and bright and mottled boulders (Sugita et al., 2019). However, as this work focuses on fractures, there was no special attention paid to boulder morphology. In contrast to previously visited asteroids, Ryugu does not have regolith-dominated areas without boulders. Ryugu's history is thought to be complex, as a rubble-pile asteroid it probably formed from the debris of a much larger (approx. 100 km), previously destroyed parent-body. It is possible that there were multiple stages of collision and that two or more parent-bodies broke apart and provided material to build Ryugu. Because of this Ryugu likely incorporated different lithologies of the original parent-bodies (Sugita et al., 2019).

The Hayabusa2 mission was launched on December 3rd, 2015 from Tanegashima in Japan to explore the near-earth asteroid Ryugu (Fig.6. The main mission objective was to return samples from Ryugu to Earth (S.-i. Watanabe et al. (2017)), which actually were successfully returned to Earth in December 2020. Hayabusa2 carried a seven-channel optical camera (ONC-T (Sugita, 2022)), a laser altimeter, a IR-Spectrometer and a thermal infrared imager. It also carried three small (10 cm) rovers, produced by Japanese Universities. A small (25 cm) lander, MASCOT (Mobile Asteroid Surface Scout), developed by the German Aerospace Research Center DLR (Ho et al., 2021), complements these instruments. The rovers and the lander were deployed on the surface of Ryugu during the 'proximity' mission phase (see table 2). Hayabusa2 also carried a explosive device called the SCI (small carry-on impactor). Using a shaped charge, this instrument allowed Hayabusa2 to simulate an high-speed impact on Ryugu's surface (Saiki et al. (2013)). Some of theses instruments are visible in Fig.6. A similar sample-return mission was also done by NASA to the near-earth asteroid Bennu, called OSIRIS-REx (Lauretta et al., 2017).

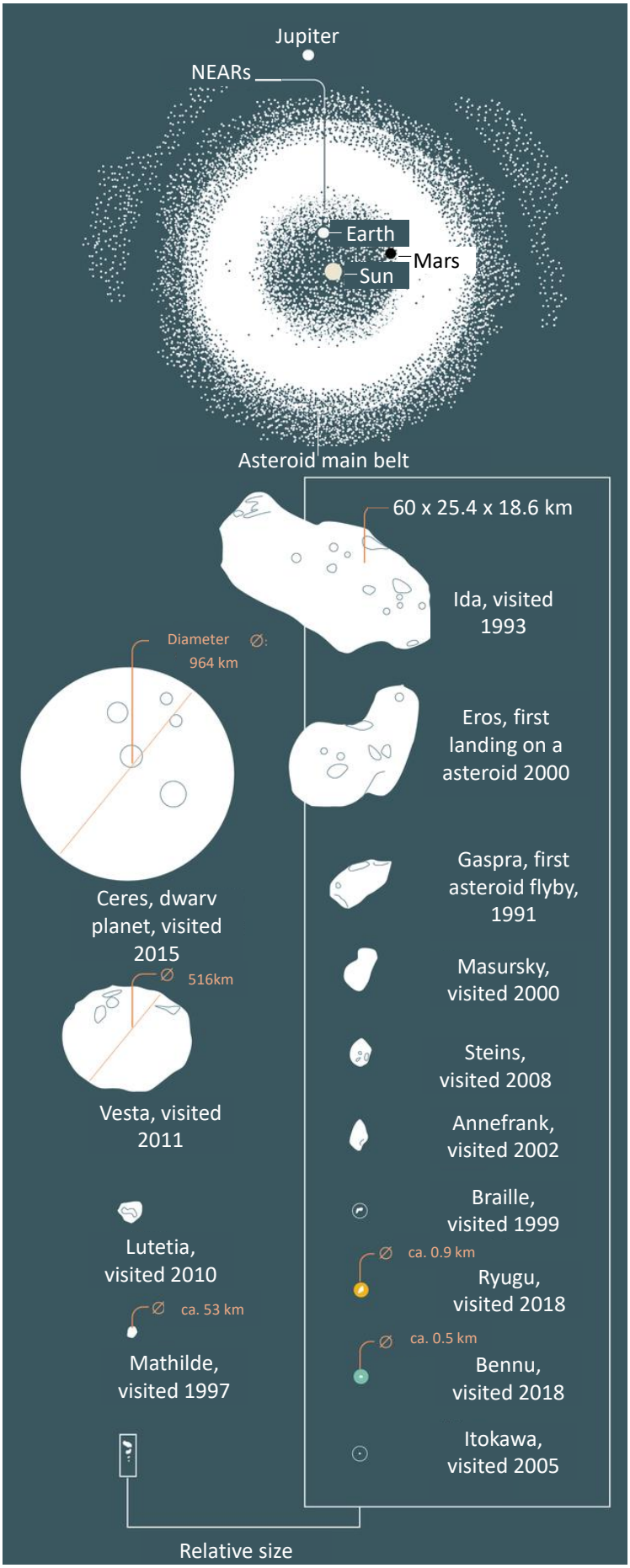

Figure 1.: Asteroids in comparison. Translated from NZZ (2020).

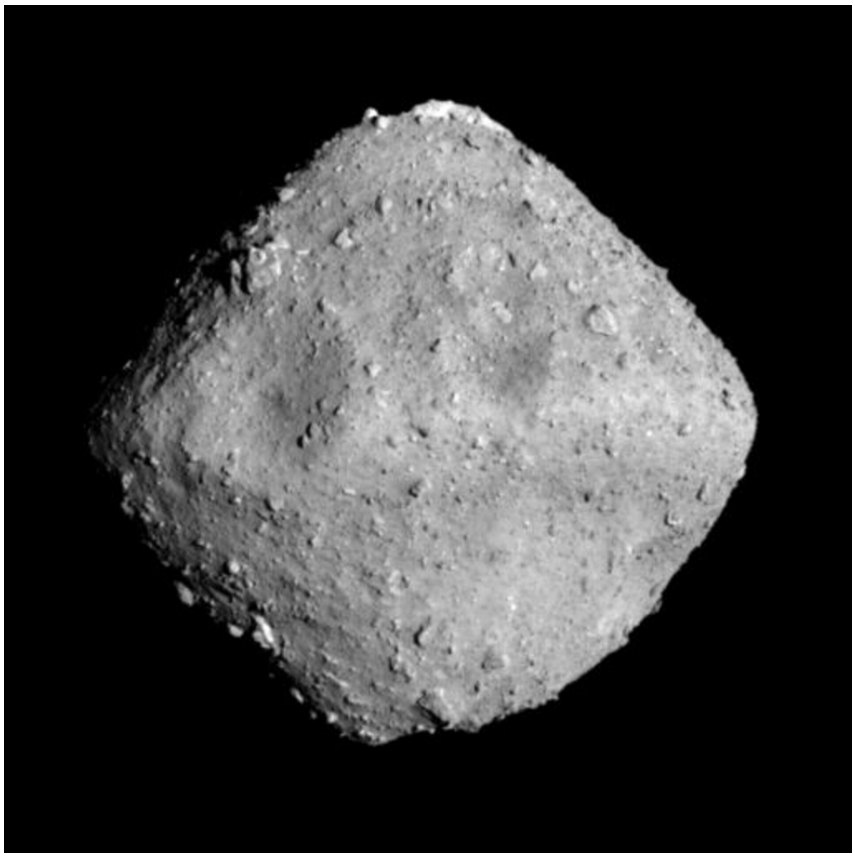

Figure 2.: Asteroid Ryugu as imaged by JAXA's Hayabusa2 mission. Credit @ JAXA Rie et al. (2022).

Name of mission phase	Period
EDVEGA (Electric Delta-V Earth Gravity Assist). From launch until Earth swing-by.	Dec. 3, 2014 - Dec. 3, 2015
Transfer	Dec. 3, 2015 - June, 2018
Approach	June, 2018 - June 28, 2018
Proximity	June 28, 2018 - Nov. 13, 2019
Return	Nov. 13, 2019 - Oct. 21, 2020
Reentry	Oct. 22, 2020 - Dec. 5, 2020

Table 2.: Hayabusa2 mission phases from Sugita (2022)

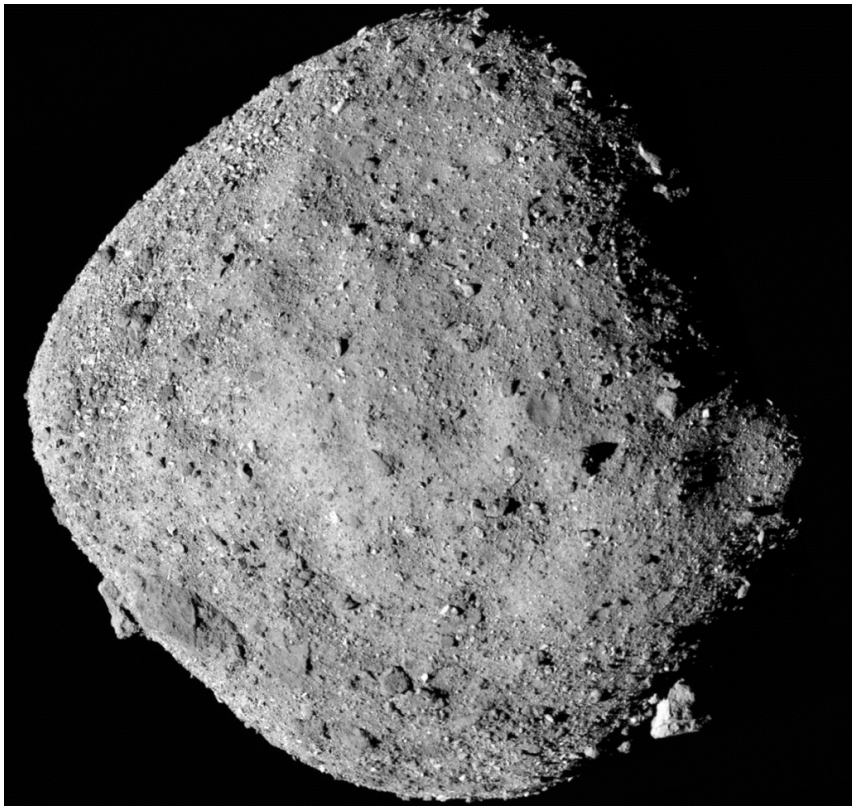

Figure 3.: Asteroid Bennu as imaged by NASA's OSIRIS-REx mission. Credit @ NASA Lauretta et al. (2017).

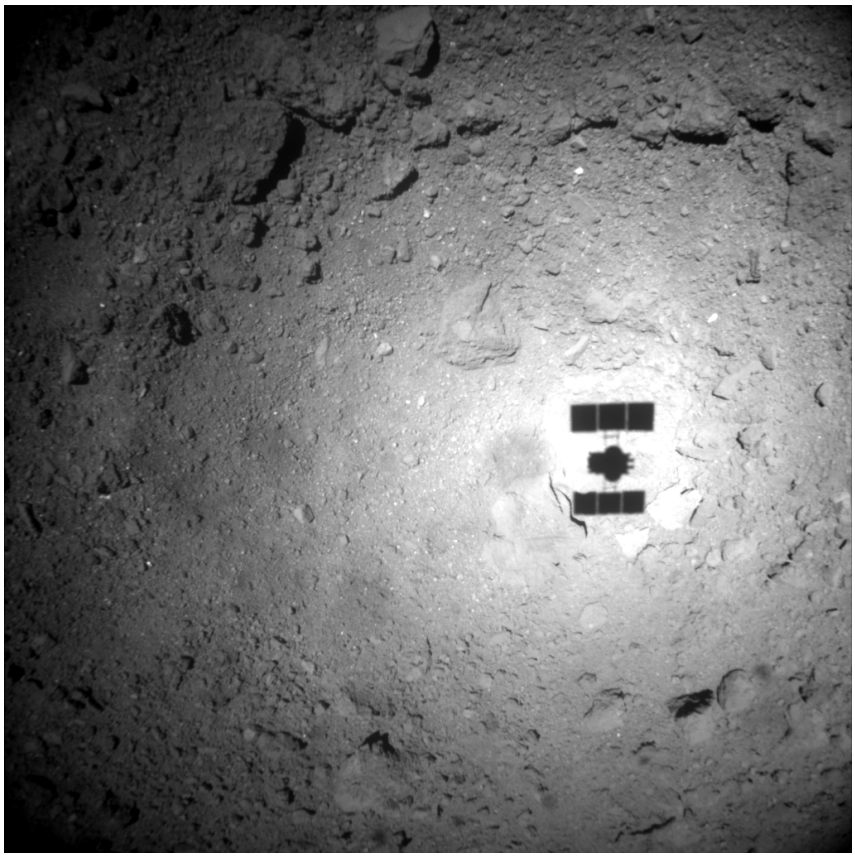

Figure 4.: High resolution image of Ryugus surface with Hayabusa2's shadow. The shadow's width is about 6 metres. Image name: hyb2_onc_20190308_032449_w1f_l2a. The apparent brightness in the center of the image is due to the opposition effect.

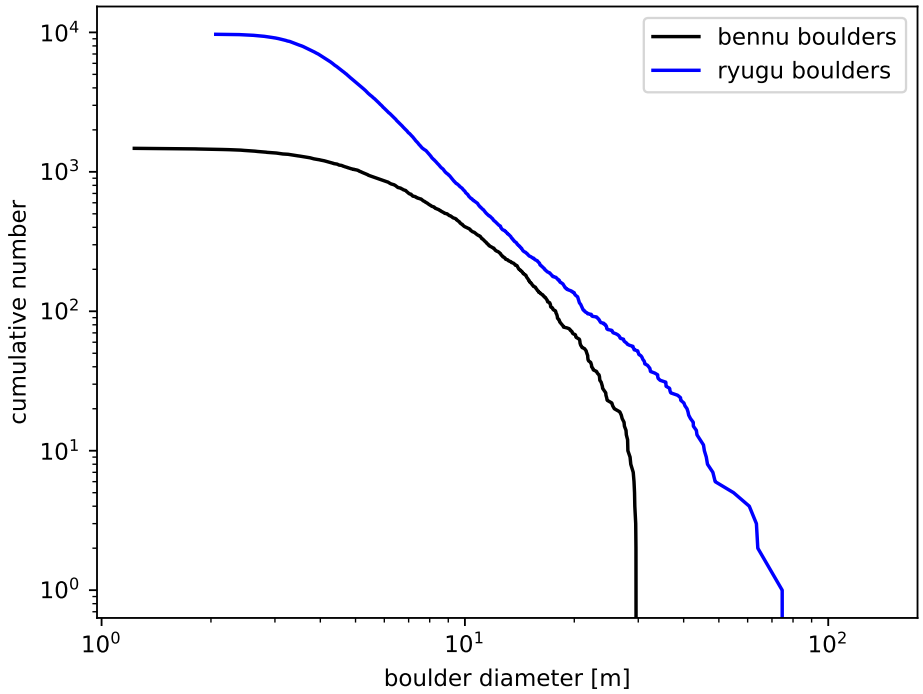

Figure 5.: Amount of boulders on Ryugu and Bennu. Data from Michikami et al. (2019) and DellaGiustina et al. (2020).

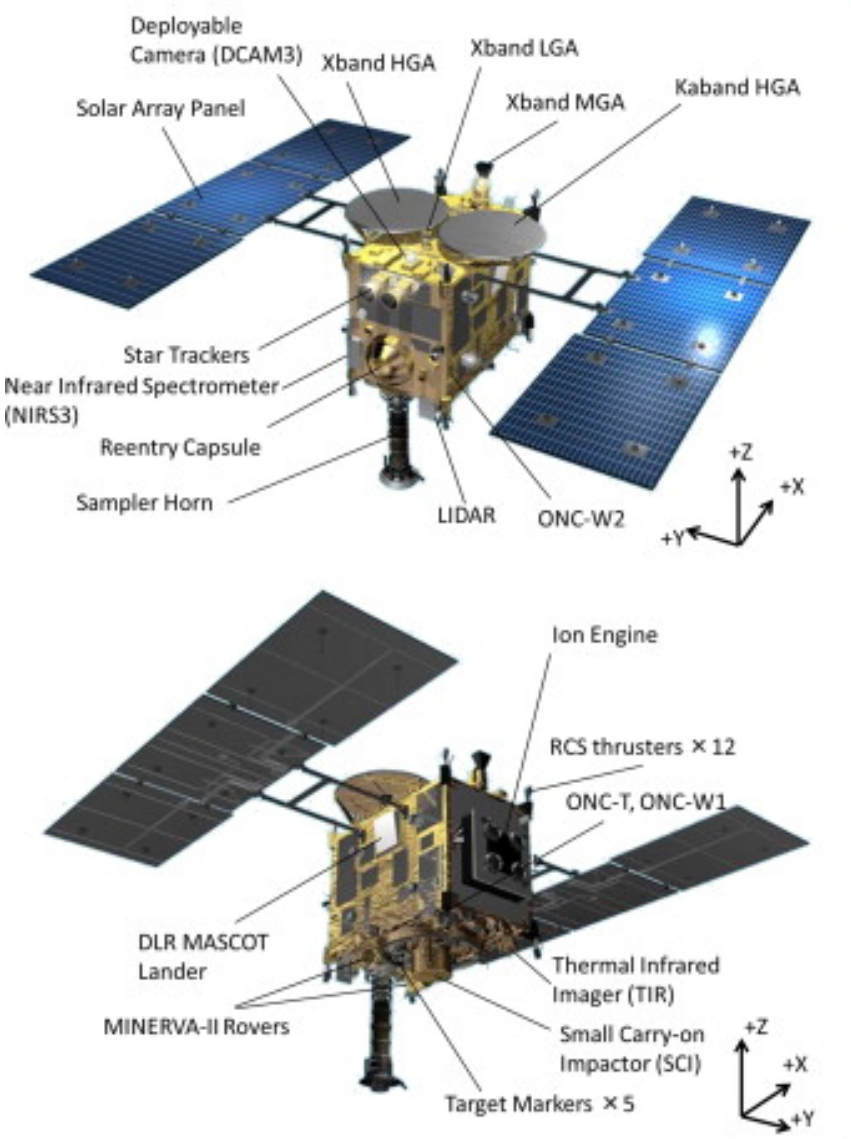

Figure 6.: External views of the Hayabusa2 spacecraft and onboard instruments, by Tsuda et al. (2013)

2.4. Bennu

To address the fundamental questions posed in chapter 1, NASA launched the OSIRIS-REx (Origins, Spectral Interpretation, Resource Identification, and Security–Regolith Explorer) mission. The primary objective of the mission was to gain insights into the formation of the early solar system by returning an asteroid sample.

More than 500,000 asteroids were considered as potential targets, with about 7,000 classified as near-earth asteroids. Among these, 192 had suitable orbits, making the mission financially feasible. To facilitate sample retrieval, asteroids smaller than 200 meters were excluded, narrowing down the candidates to 26 possible targets. Only 5 of these candidates exhibited a carbonaceous, primitive composition—a sign of little alteration—making them ideal candidates for study. Bennu emerged as the most well-characterized asteroid, primarily due to detailed astronomical observations, leading to Bennu's selection for the OSIRIS-REx mission (Lauretta et al., 2017).

Bennu, a near-earth rubble-pile asteroid with a diameter of about 500 meters, has a spheroidal shape and a visually striking equatorial ridge (see Fig. 3), likely formed by rotational forces. Categorized as a B-type asteroid, it belongs to the spectrally bluer subclass of C-type carbonaceous asteroids mentioned earlier.

OSIRIS-REx boasts a plethora of instruments, this includes three spectrometers, several cameras, a laser altimeter and a sample retrieval mechanism, operating with nitrogen gas (Ajluni et al., 2015). These are visible in Fig. 7.

When OSIRIS-REx arrived at Bennu in 2018 the surface of Bennu was unexpectedly rough and rocky (Lauretta et al., 2019). This was a significant challenge for the mission team, since the asteroid was expected to have a smooth surface with small-grained regolith. A rocky surface makes the approach of the spacecraft, to collect a sample, much more difficult. However these challenges where overcome, allowing a sample to be taken in 2020 (Lauretta et al., 2021). This sample is projected to arrive on Earth in September 2023, where it will be meticulously analysed.

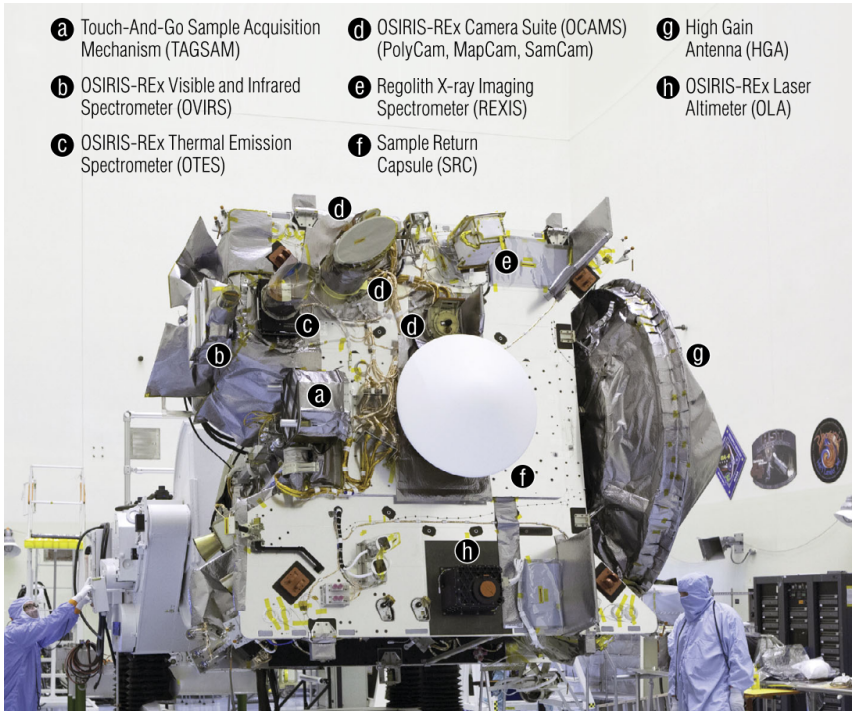

Figure 7.: External views of the OSIRIS-REx spacecraft and onboard instruments, by Lauretta et al. (2017).

2.5. Thermal Fracturing

To acquire a better understanding of the environment and processes that form and shape Ryugu and similar small bodies, studies have tried to demonstrate and quantify the influence of the thermal environment on the development of asteroids landscapes (Delbo et al. (2022)). One area of research that has received significant attention is thermal fracturing, which is the process of cracking and breaking of rocks due to temperature changes induced by the different exposure to the sun during rotation. On small bodies like Ryugu, thermal fracturing can occur when the surface experiences rapid changes in temperature, such as when the asteroid rotates and exposes different regions to sunlight and shadow. Non-thermal processes that could induce fracturing are (micro-)impact or gravitational effects.

Through laboratory experiments and numerical simulations, researchers have found that thermal fracturing can lead to the formation of various surface features on small bodies, including boulders, rocks, and regolith. The size and distribution of these features can provide clues about the thermal history of the asteroid, as well

as its physical properties and structural characteristics (Delbo et al. (2014)).

By studying the spatial distribution of these features and their relationship with the asteroid's topography, researchers can infer the extent of thermal fracturing that has occurred on Ryugu and how it has influenced the asteroid's landscape.

Thermal fracturing is therefore a key process that shapes the surface of small bodies like Ryugu, and studying its effects can provide valuable insights into the geological history of these objects and the physical processes that govern their evolution.

3. Methods

3.1. Identification and mapping of fractures

In this thesis images from the HAYABUSA-2 Optical Navigation Camera (ONC (Sugita, 2022)) were used to identify fractures in Fig.8. A fracture on a boulder was usually identified as a dark linear feature, since the sunlight usually does not illuminate the fracture entirely.

However, the visual identification of fractures is prone to errors, since fractures are not the only linear features that produce shadows. Boulder boundaries or pre-existing features in the rock can be mistaken for fractures. To avoid this ambiguity, the mapped fractures were divided into three groups, describing the fracture confidence level (see table 5 in chapter 4): (i) one group that only contains features that are definitely and obviously fractures given their morphologic appearance (e.g. properly split boulders or comparatively wide fractures); (ii) one larger group, that contains all group-one features plus some fractures, that might only be shadows; and (iii) the largest group containing more than tenfold the amount of features in the other groups, with features that are often hard to identify correctly and therefore might not all be fractures, see Figs. 10, 11, 12 and 13.

The fractures were mapped by drawing a multi-line shapefile in QGIS (QGIS Development Team (2023)), as a fracture usually consists of multiple segments. The aim of this work is to apply the mapping done by Delbo et al. (2022), based on OSIRIS-REx data from asteroid Bennu in Fig.9, to a second asteroid, Ryugu. However the mapping was not exactly reproducible like outlined in Delbo et al. (2022), because they worked on a global high-resolution data set by Bennett et al. (2021), which is not available for Ryugu.

Instead, I selected Hayabusa2 images via their fly-by distance to Ryugu. I have

chosen images from the proximity phase in the Hayabusa2 mission (see table 2), where the distance between the Hayabusa2 spacecraft and Ryugu was less than 1 km, leading to a best-case resolution of 10 mm/pixel (Kameda et al., 2016). I then map-projected these images using a equidistant cylindrical projection (see Longley et al. (2005)). Here problems arose: the spice kernels(NASA Navigation Ancillary Information Facility, 2023), that contain the needed telemetry data to project the images are damaged. This contains data such as spacecraft-, instrument- and mission-target location and orientation in their respective coordinate system. Spice kernels are usually used by NASA to plan and interpret space mission data. But since they were corrupted, so called "geocubes" were used to map-project images (Rie et al., 2022).

These geocube files (file-ending: .dbpc) contain the information which pixel is at which latitude and longitude on Ryugu and are provided by the Japanese Space Agency. However, the quality of these geocubes was variable. Some of the images are perfectly projected, thus one picture smoothly overlaps into the next picture without any problems. Most of the images were projected reasonably well, where some minor displacements between different pictures are visible, but on a negligible scale. And then some of the geocube files contained such corrupted information that images that show the same geographic features were projected onto completely different locations on the map. This resulted in 198 correctly projected images, listed in A, from 457 in total that were taken below 1 km. These are the pictures on which the actual mapping took place (Fig. 8).

3.2. Data Processing

Once the mapping was done, the fracture coordinates were exported in QGIS. This data was then read and processed with Python. The lengths l_i of the fracture segments were obtained via the euclidean norm on the map-projected images, see equation 3.1. This assumes Ryugu is spherical, which Ryugu is not (see Fig.2), but since the fractures are small (cm - m), the resulting error is negligible. After this, the segment-lengths were summed up to compute the total length of a fracture. The

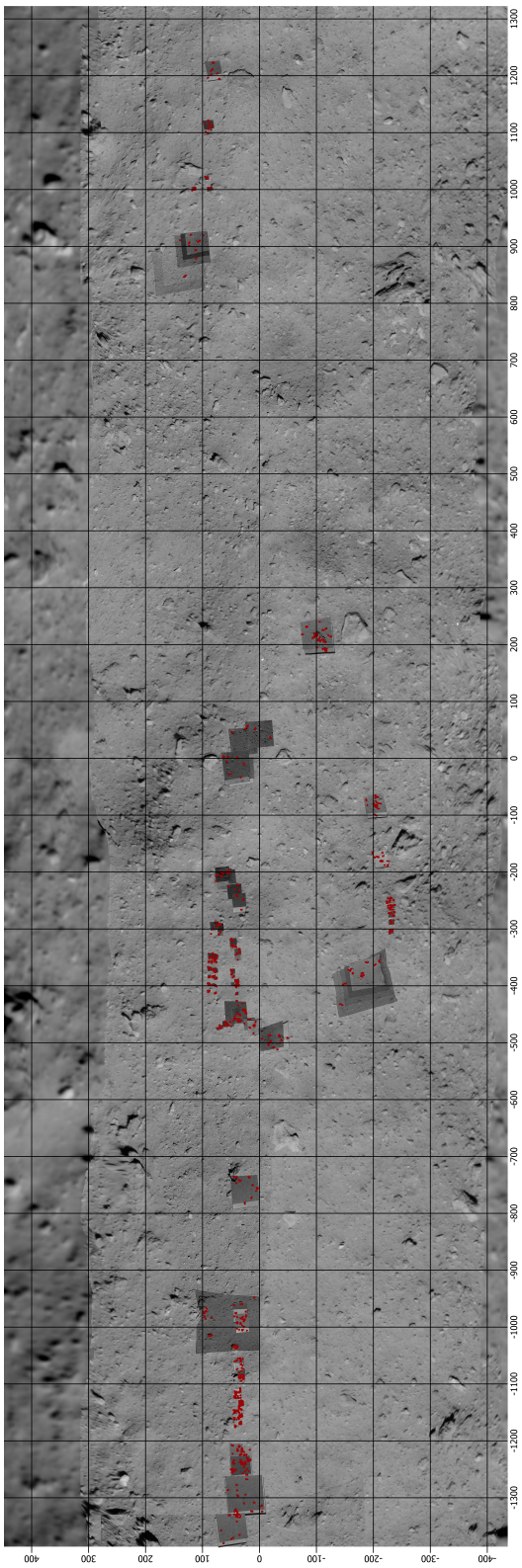

Figure 8.: Global map of Ryugu. Red markings are fractures, mapped on available high-resolution images. This image is a compilation of a global Ryugu mosaic and the high-resolution images I worked on, see A. It is rotated for better visibility, so north is to the left, east to the top. Since the underlying equidistant coordinate system is in metres, the displayed grid is in metres too.

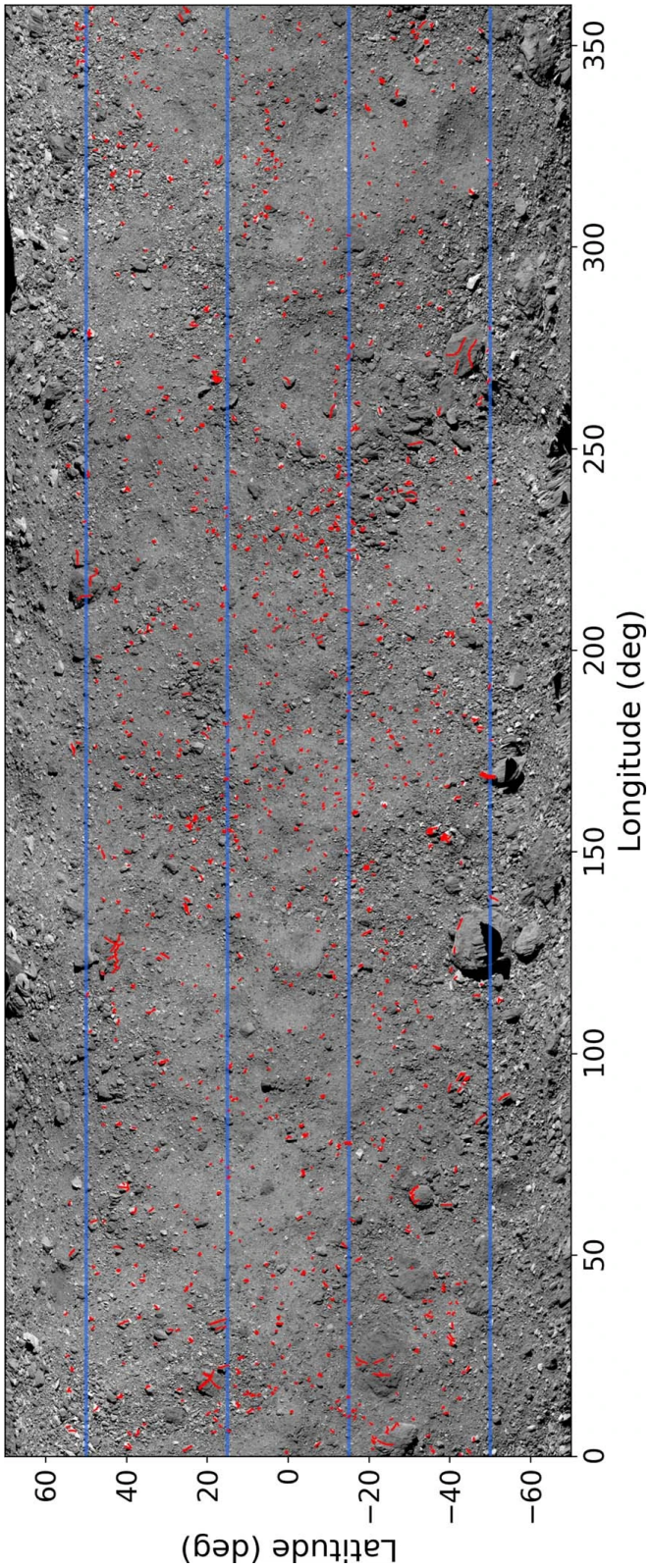

Figure 9.: Global map of Bennu by Bennett et al. (2021). Red markings are fractures mapped by Delbo et al. (2022). This image was rotated for better visibility, so north is to the left, east to the top.

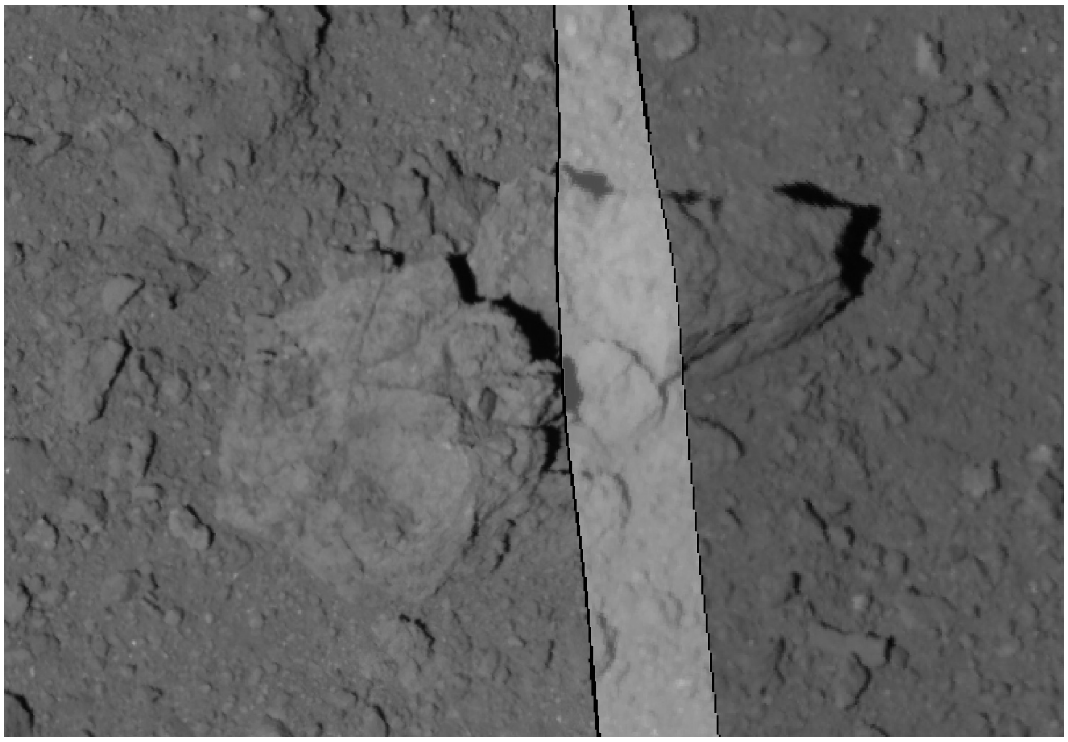

Figure 10.: Mapping example, with no mapped fractures, for reference. Composition of 3 Hayabusa2 images: hyb2_onc_20180921_025306_tvf_l2d, hyb2_onc_20181015_140115_tvf_l2d and hyb2_onc_20181015_140218_tuf_l2d. The image width is approx. 30 m.

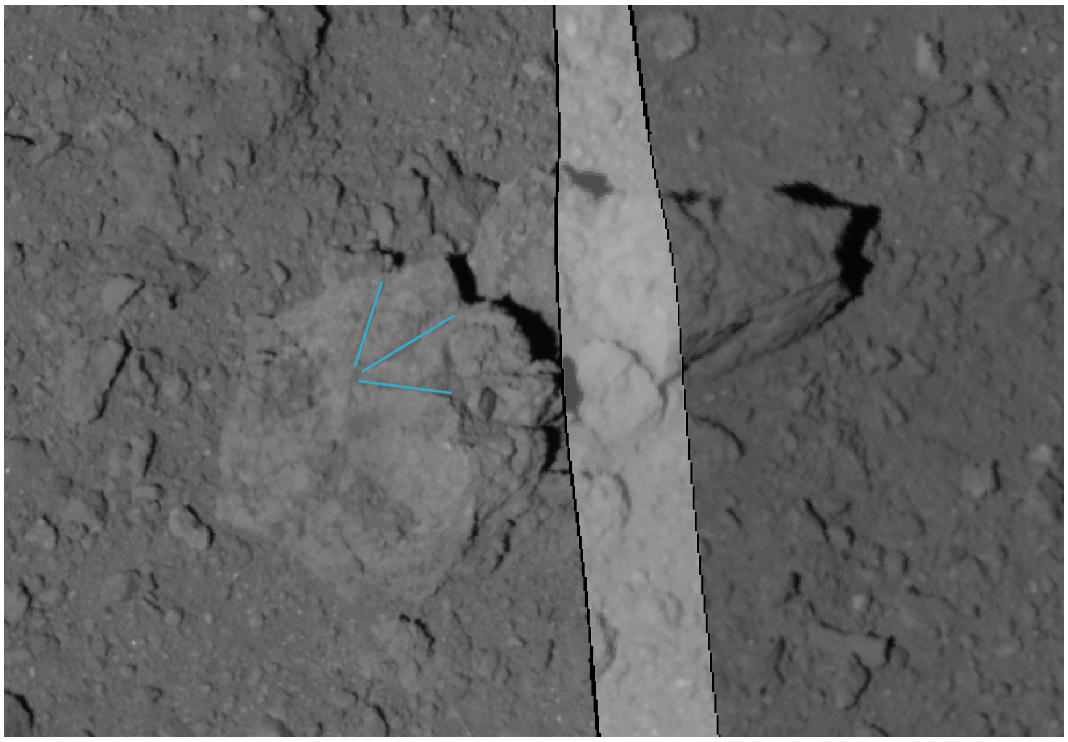

Figure 11.: Mapping example, with fractures of group 1 in blue. Composition of 3 Hayabusa2 images: hyb2_onc_20180921_025306_tvf_l2d, hyb2_onc_20181015_140115_tvf_l2d and hyb2_onc_20181015_140218_tuf_l2d. The image width is approx. 30 m.

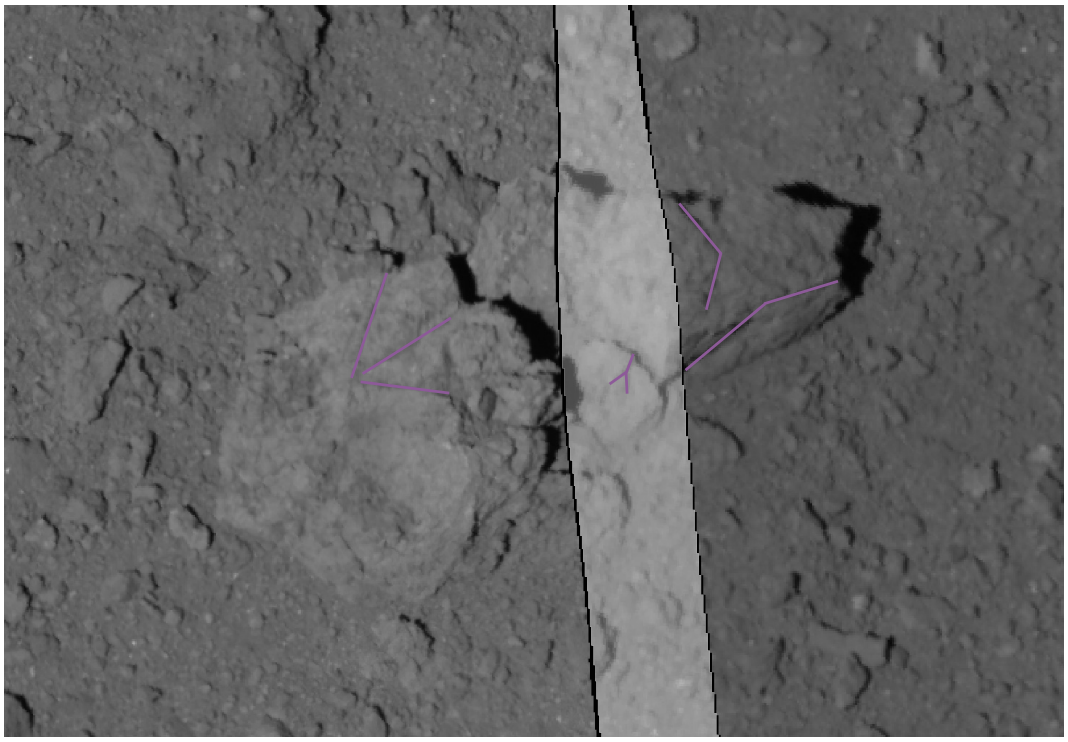

Figure 12.: Mapping example, with fractures of group 2 in violet. Composition of 3 Hayabusa2 images: hyb2_onc_20180921_025306_tvf_l2d, hyb2_onc_20181015_140115_tvf_l2d and hyb2_onc_20181015_140218_tuf_l2d. The image width is approx. 30 m.

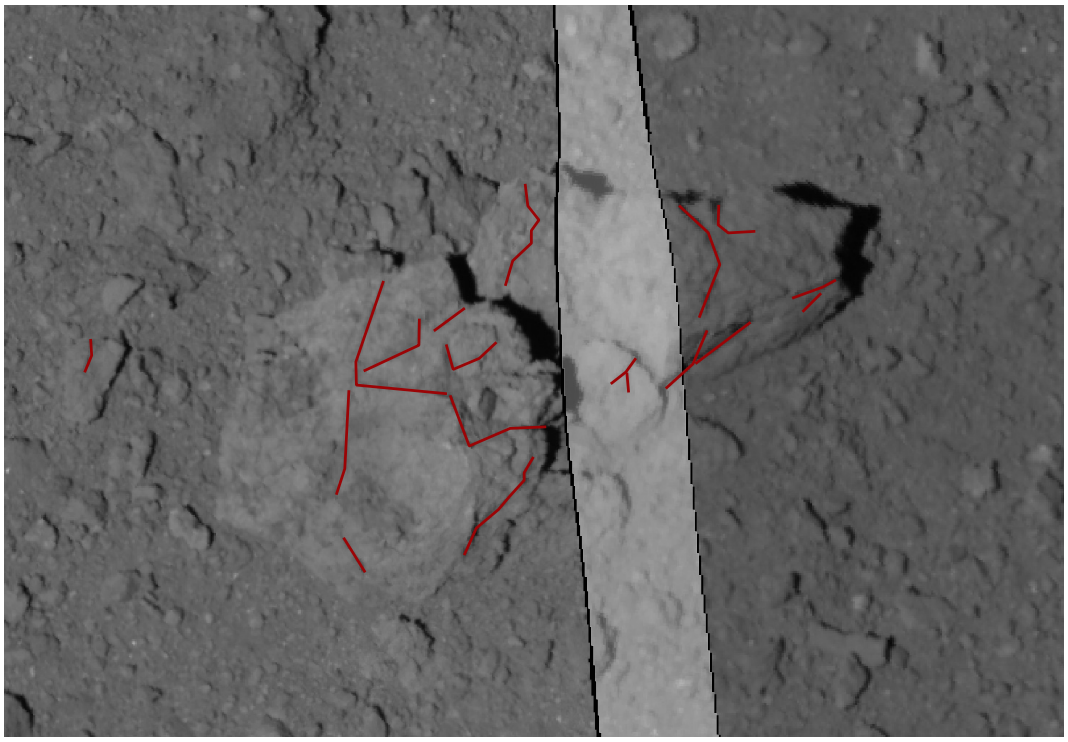

Figure 13.: Mapping example, with fractures of group 3 in red. Composition of 3 Hayabusa2 images: hyb2_onc_20180921_025306_tvf_l2d, hyb2_onc_20181015_140115_tvf_l2d and hyb2_onc_20181015_140218_tuf_l2d. The image width is approx. 30 m.

orientation α_i of a fracture is calculated with equation 3.2 via the difference of the respective X and Y coordinates of the fracture-segment-points, again assuming a spherical body with a radius of 450 m.

$$l_i = \sqrt{(x_2 - x_1)^2 + (y_2 - y_1)^2} \tag{3.1}$$

$$\alpha_i = \arctan(x_2 - x_1, y_2 - y_1) \tag{3.2}$$

Once all fracture orientations have been calculated, they were plotted in rose diagrams. The length distribution plots in section 4.2 were done by plotting the cumulative sum of the fractures against their length in a double logarithmic plot.

3.3. Fracture Propagation Model

The fracture-propagation model of Delbo et al. (2022) was used to model fracture growth on Ryugu. It allows to estimate the time scale in which Ryugu's current surface was formed. To apply this model to Ryugu, different parameters had to be used, most notably the rotational period of 7.633 hours (differs from Bennu's 4.296 hours) resulting in a measured daily temperature variation of 97° K(Grott et al., 2019). To correctly estimate other thermo-physical properties of the boulders on Ryugu (and Bennu) is no easy task, since even the properties for different boulders on Ryugu can vary quite significantly (Sakatani et al., 2021). Nevertheless, important parameters from the literature are compiled in table 3 and comprise results from Hayabusa2's MARA radiometer (Grott et al., 2019) and laboratory measurements on Ryugu samples by Hayabusa2 (Nakamura et al., 2023). In accordance with Delbo et al. (2014), Paris law's exponent and prefactor (see equation 3.3) as well as the Poisson ratio ν were taken from generic CI-chondrites. The final model parameters used in this thesis are listed in table 4.

In the methods section of Delbo et al. (2022), their fracture-propagation model is described in detail. The relevant parts are repeated here. The geometry of the model is adopted from Delbo et al. (2022). In Fig.14 a modelled boulder (green) rests in

Source Body	Grott et al. (2019) Ryugu	Nakamura et al. (2023) Ryugu
Density, ρ	1270*	1790
Heat capacity, C_p	600/1000	865
Thermal Inertia, Γ	282	-
Thermal expansion coefficient, α	-	2.6e-5
Poisson ratio, ν	-	-
Rotation period, P	7.6326	-
Young modulus, E	10	5.3
Temperature difference,ΔT	97	-

Table 3.: Ryugu's parameters compiled for the fracture-propagation model
*this is Ryugu's average density, with porosity included

Source Body	Unit	Delbo et al. (2022) Bennu	This work Ryugu
Density, ρ	$kg * m^{-3}$	2236	2236*
Heat capacity, C_p	$J * kg^{-1} * K^{-1}$	1000	865
Thermal Inertia, Γ	$J * m^{-2} * K^{-1} * s^{-0.5}$	370	282
Thermal expansion coefficient, α	K^{-1}	5e-6	2.6e-5
Poisson ratio, ν		0.2	0.2
Rotation period, P	h	4.296	7.636
Young modulus, E	GPa	10	5.3
Temperature difference, ΔT	K	70	97

Table 4.: Parameters used for the fracture-propagation model
*since the measured density values are not pure pure grain-density, but bulk-density with (micro)-porosity included, the estimated grain-density by Delbo et al. (2022) was used

regolith (grey) with the dashed yellow/black rectangle being the growing fracture. The boulder is a cylinder with radius D and length $2L_x$. The fracture horizontal length is $2a_x$ and it penetrates the boulder to a depth of $2a_z$.

The model is based on Paris (1961) Law, which computes the fracture growth per thermal cycle:

$$\frac{da}{dN} = C[\Delta K_I]^n \tag{3.3}$$

Where N is the number of thermal cycles, n and C are Paris law's exponent and prefactor, respectively. With values of 0.0003 for C and 3.84 for n are taken from Delbo et al. (2014). K_I is the stress intensity factor (see Delbo et al. (2014), Ravaji et

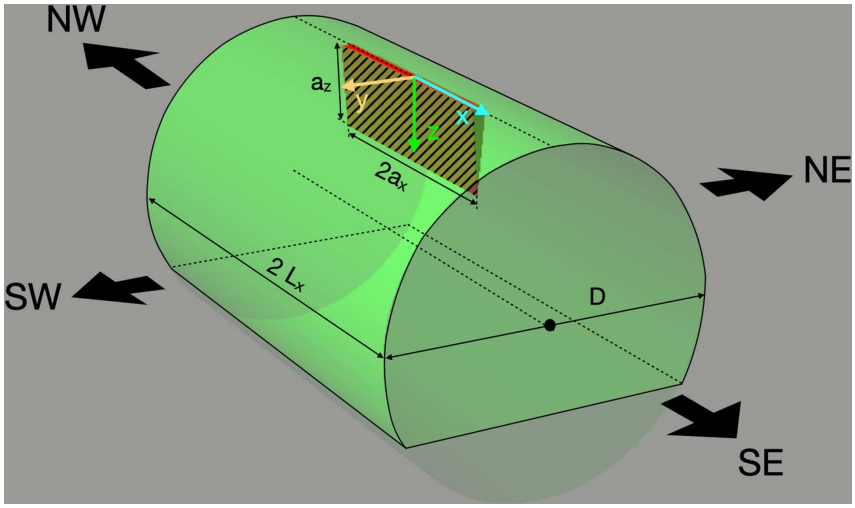

Figure 14.: Model geometry, from Delbo et al. (2022)

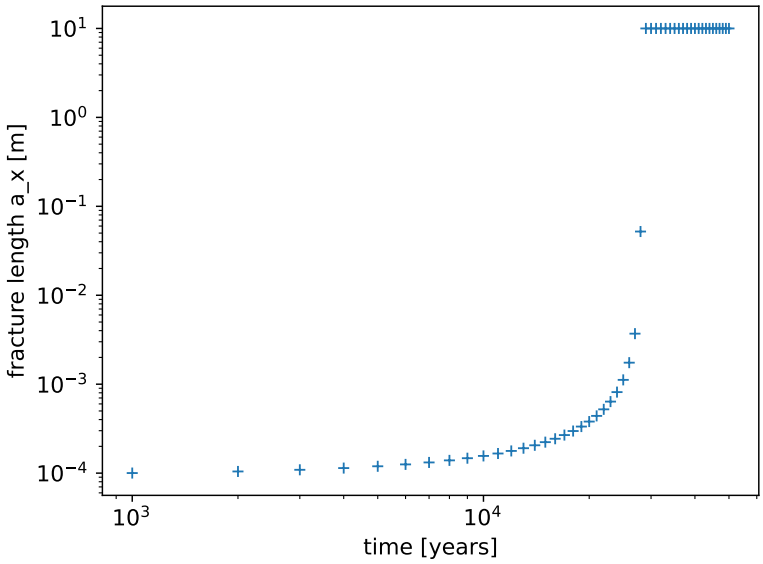

Figure 15.: The simulated growth of a singular fracture over 50.000 years on Bennu. In a boulder that has a diameter of 2 m and a Length of 10 m. After about 30.000 years the maximum Length of 10 m is reached and the fracture can not grow further.

al. (2019) and El Mir et al. (2019)) and a is the fracture length (here in x-direction). The stress intensity factor can be calculated following the solution for a through fracture in a plate (Cartwright & Rooke (1975)):

$$K_I = \frac{f\left(\frac{a}{L}\right)}{\sqrt{\pi a}} \int_0^a dx \frac{\sqrt{a+x}}{\sqrt{a-x}} \sigma_{yy} \tag{3.4}$$

Where $f\left(\frac{a}{L}\right)$ is a geometric correction factor:

$$f\left(\frac{a}{L}\right) = \left(1 - \frac{a}{L} + 0.326\frac{2a}{L}^2\right)\left(1 - \frac{2a}{L}\right)^{-0.5} \tag{3.5}$$

The thermal stress σ_{yy} consists of a macroscopic $\sigma_{yy}^{l_s}$ and a microscopic part σ_{yy}^{TM}:

$$\sigma_{yy} = \sigma_{yy}^{l_s} + \sigma_{yy}^{TM} \tag{3.6}$$

However, the direction of the microscopic stress reverses at each chondrule-matrix boundary (see section 2.2) and therefore is mostly cancelled out and ignored in this work. The macroscopic part is described in Ravaji et al. (2019) as:

$$\sigma_{yy}^{l_s} = \frac{Q\alpha E \Delta T_s}{6(1-\nu)}\left(e^{\frac{-z}{l_s}} - \frac{l_s}{D}\left(1 - e^{\frac{-D}{l_s}}\right) + 3\frac{l_s}{D}(2\frac{z}{D} - 1)\left(2 - (2\frac{z}{D} + 1)\left(1 - e^{\frac{-D}{l_s}}\right)\right)\right) \tag{3.7}$$

Where $Q = max\left(\frac{1}{3}, \frac{3}{4}\frac{D+4l_s}{D+12l_s}\right)$ is a geometric correction factor, α the thermal expansion coefficient, $l_s = \sqrt{\kappa P/\pi\rho C_p}$ is the diurnal thermal skin depth (usually few centimeters on Ryugu), κ the thermal conductivity, ρ density, C_p the specific heat capacity and ν Poisson's ratio of the boulder material. The thermal conductivity can be calculated via equation 3.8, where Γ is the Thermal Inertia:

$$\kappa = \frac{\Gamma^2}{\rho C_p} \tag{3.8}$$

Then equation 3.4 can be analytically integrated with $\sigma_{yy} \approx \sigma_{yy}^{l_s}$:

$$K_I = \sigma_{yy}^{l_s}\sqrt{\pi a} f\left(\frac{a}{L}\right) \tag{3.9}$$

This makes it possible to solve equation 3.3 in its entirety, allowing us to calculate the fracture growth per thermal cycle by using the asteroid's rotational period as duration of the thermal cycle. The parameters used are listed in table 4. For most parameters a measured value from Nakamura et al. (2023) or Grott et al. (2019) was available, which was deemed better than estimated values and therefore used. However, the reported density by Nakamura et al. (2023) and Grott et al. (2019) was not utilized in the analysis. The model does not account for porosity, whereas the measured values include porosity alongside pure grain density, which is the reason for not incorporating the reported values. For the Poisson ratio ν no measurements were available, so the previous from Delbo et al. (2022) was used.

The model starts with a random log-normal distribution of micro-fractures of a specific length, in this case the values range from 10^{-6} m to 4×10^{-4} m, approximating measured values in meteorites by Bryson et al. (2018). Every micro-fracture gets assigned a random boulder size below 30 m, from the observed values in Bennu's or Ryugu's boulder distribution (DellaGiustina et al. (2020) and Michikami et al. (2019)). Then the individual horizontal growth for each fracture is calculated in 10-year time-steps from equation 3.3. At the end of the model calculation, we obtain a new fracture distribution after the set model duration. The evolution of a singular fracture over time is plotted in Fig. 15.

4. Results

4.1. Fracture Orientation

The mapping resulted in three QGIS shape-files based on the quality of the fracture identification, listed under "confidence" in table 5 . They contain 47/128/1521 fractures, with a total of 97/246/4195 fracture-segments. The orientation of the segments were computed as in equation 3.2 and are plotted in figures 16, 17 and 18. Figure 16 shows a slight preferred North-South orientation. Figure 17 seems to show a East-West orientation. Figure 18 however shows a very strong and unambiguous North-South orientation. More than 66% of fractures here are oriented directly North-South (with a maximum deviation of 15 degree from a true North-South orientation). This mirrors the results of Delbo et al. (2022), which is further discussed in chapter 5.

	Group 1	Group 2	Group 3
confidence level	high	immediate	low
amount of fractures	47	128	1521
amount of segments	97	246	4195
approximate orientation	North-South	East-West	North-South

Table 5.: Three groups of detected fractures

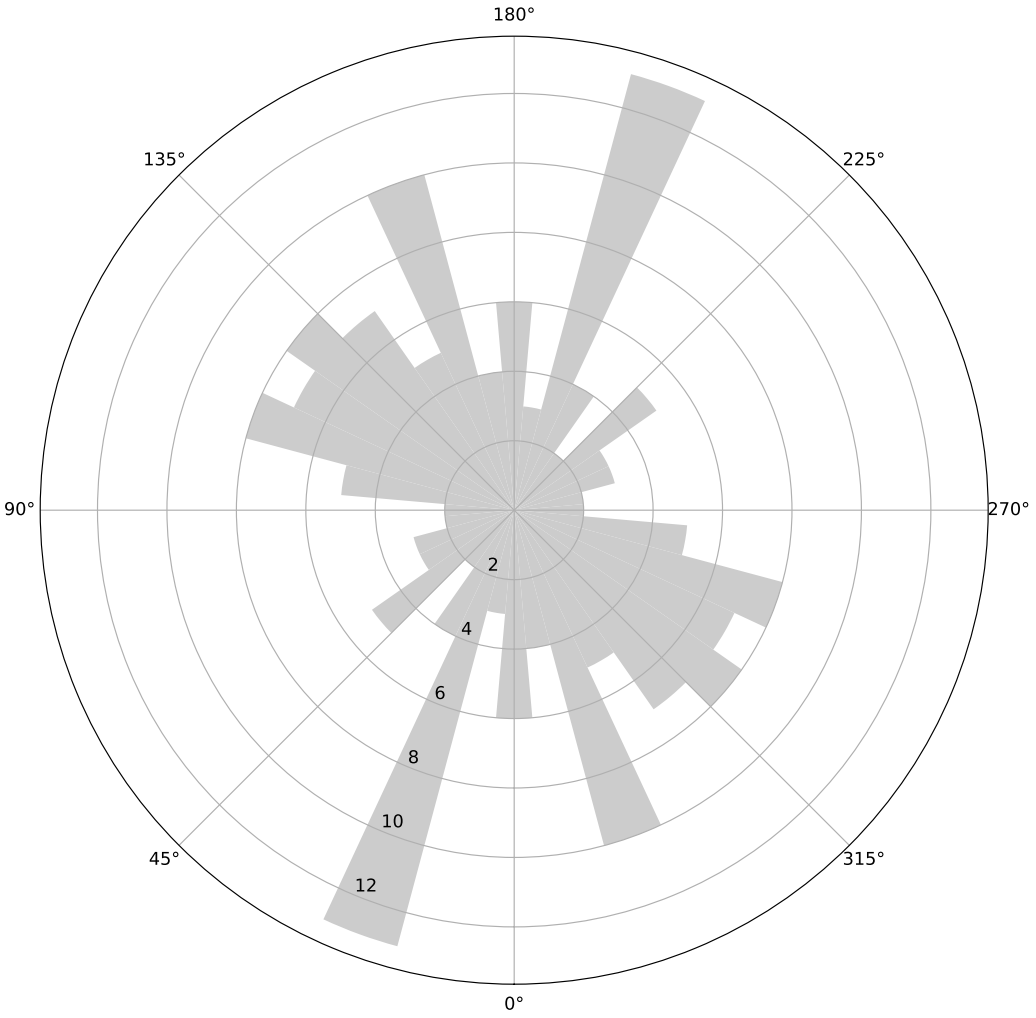

Figure 16.: Fracture orientation of group one, north is up. This could be interpreted to be a preferred North-South orientation, but note the small sample size. The largest bin only contains 13 fractures.

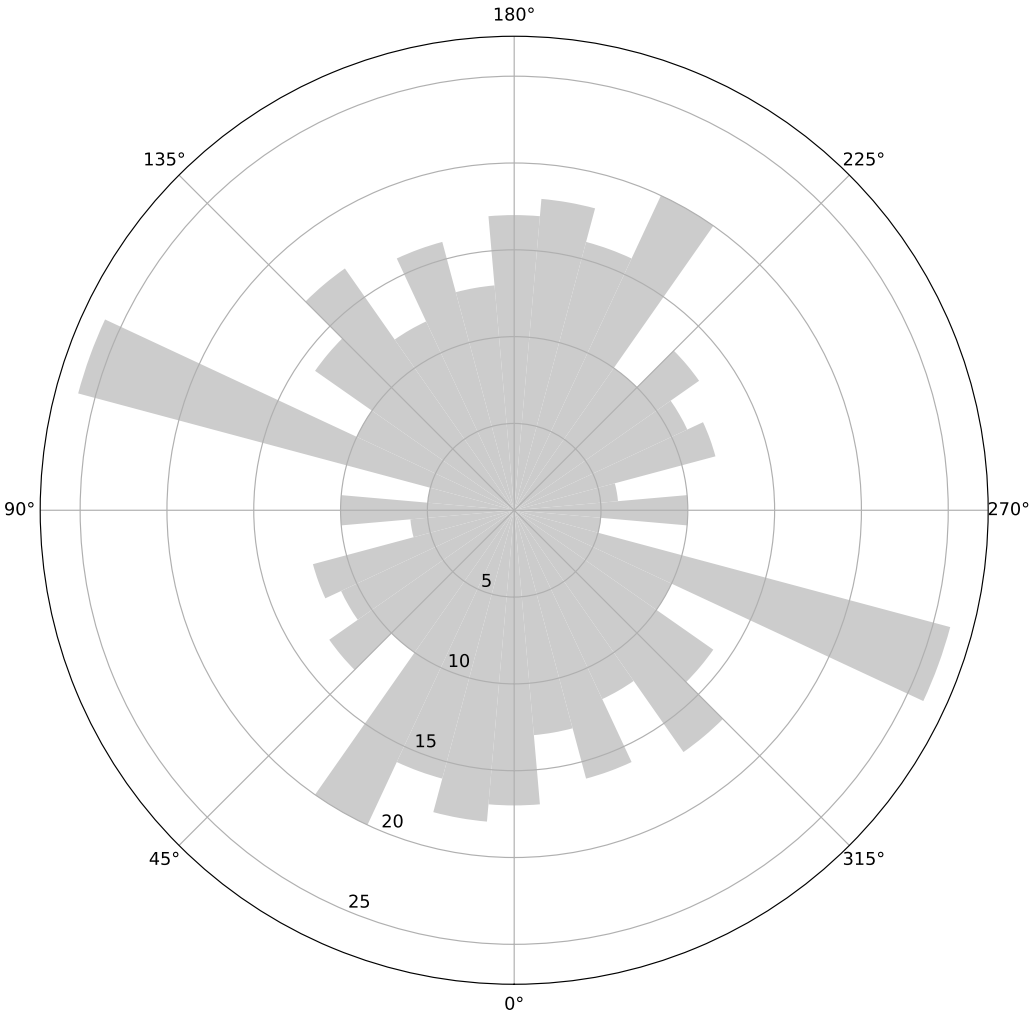

Figure 17.: Fracture orientation of group two, north is up. This could be interpreted to be a preferred East-West orientation, but it is only one notable bin.

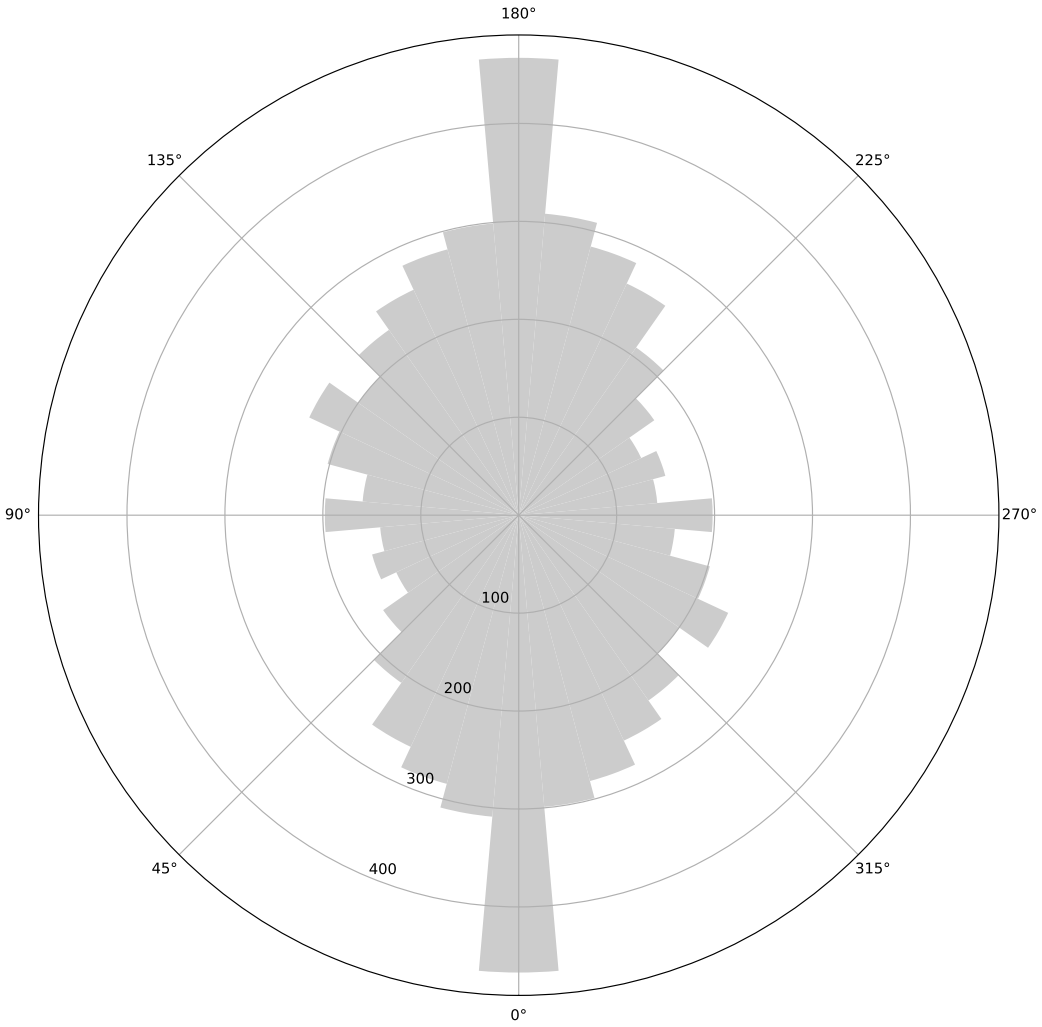

Figure 18.: Fracture orientation of group three, north is up. With strong North-South preference. About 500 fractures are oriented directly North-South, note that the North-South adjacent bins are also larger.

4.2. Length Distribution

Following Delbo et al. (2022) the fractures were also evaluated regarding their length. Figure 19 is a reproduction of Figure 3 from Delbo et al. (2022), with our Ryugu fracture data added.The graph shows the cumulative number of fractures and fracture segments plotted against their length. The data by Delbo et al. (2022) produced from Bennu (black and gray in Fig. 19) and the data I produced from Ryugu are similar, indicating that a partial mapping is enough to discover the underlying length distribution. I.e. even tough the mapping that took place for this work was not done with a global data set of Ryugu (see section 3.1), the length distribution that was found is still very similar to the global mapping by Delbo et al. (2022).

This also suggests, that the observed length distributions in Fig. 19 can be split in two parts depending on the fracture size (see Fig. 20): the fracture lengths above approximately 3 to 4 meters can be described by a power-law, the fracture length below 3 to 4 meters can be described with an exponential law. Since the largest fractures can only ever be as long as the diameter of the fractured boulder and since the boulder size frequency distribution is governed by a power-law (Michikami et al. (2019)), the fracture size above a certain size has to be too. Below this threshold, the fracture lengths can be described by a exponential law, which was also found on comet 67P by Attree et al. (2018) and Matonti et al. (2019) and thought to be typical for a thermal origin. At the lowest end of the fracture length distribution there is also a small part which is not described well by the exponential law, which is due to the resolution limit of the images, at which the fractures can not be detected reliably.

The fracture length distribution of Ryugu is described with the power law $N = N_0 L_x^{\gamma}$ with $N_0 = 988$ and $\gamma = -2.72$ and the exponential law $N = N_1 exp(L_x \beta)$ with $N_1 = 1788$ and $\beta = -1.475$, compared to $\gamma = -2.4$ and $\beta = -0.585$ from Delbo et al. (2022). Michikami et al. (2019) found a $\gamma = -2.65$ for the boulder diameter distribution on Ryugu, which is in good agreement with our fracture length value of $\gamma = -2.72$. It is worth to note that even though Ryugu's surface was only mapped partially, a very similar amount of fractures was found compared to the global mapping on Bennu. This might be explained by Bennu's smaller size, with Bennu's di-

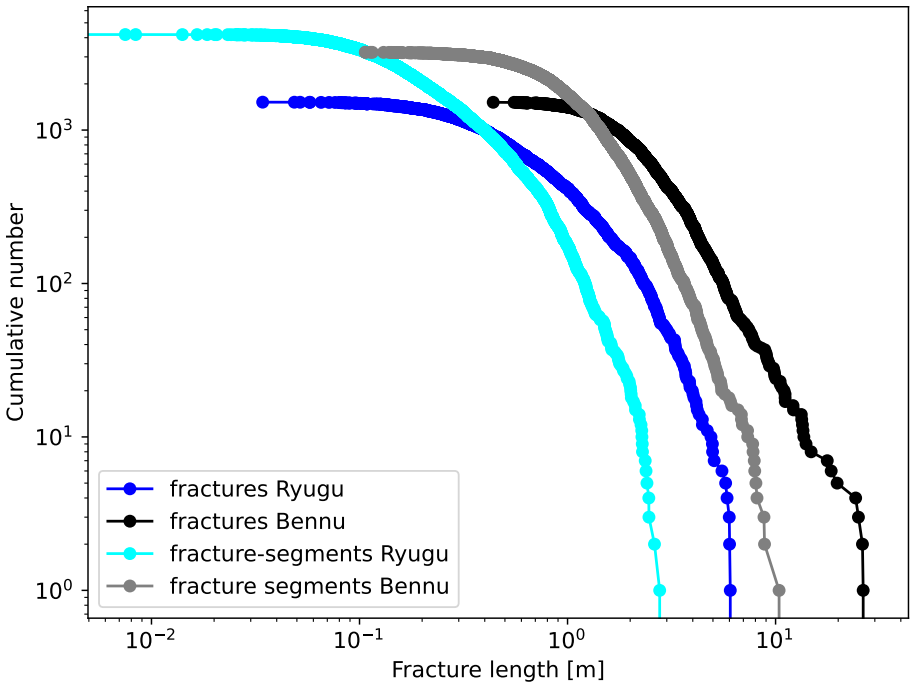

Figure 19.: Cumulative distribution of the length of fractures and fracture segments. The grey and black curves are from Delbo et al. (2022), blue curves are from Group 3 on Ryugu.

ameter being slightly larger than half of Ryugu's diameter, leading to Bennu having less than a third of Ryugu area. Note that these fit parameters change when the graph is normalized. However since the amount of observed fractures is very similar, 1475 on Bennu, 1521 for Ryugu, the change only occurs in the fifth decimal and therefore is ignored.

Source	Delbo et al. (2022)	This work
Body	Bennu	Ryugu
exponent of power law	$\gamma = -2.4$	$\gamma = -2.72$
exponent of exponential law	$\beta = -0.585$	$\beta = -1.475$

Table 6.: Parameters of the individual fits

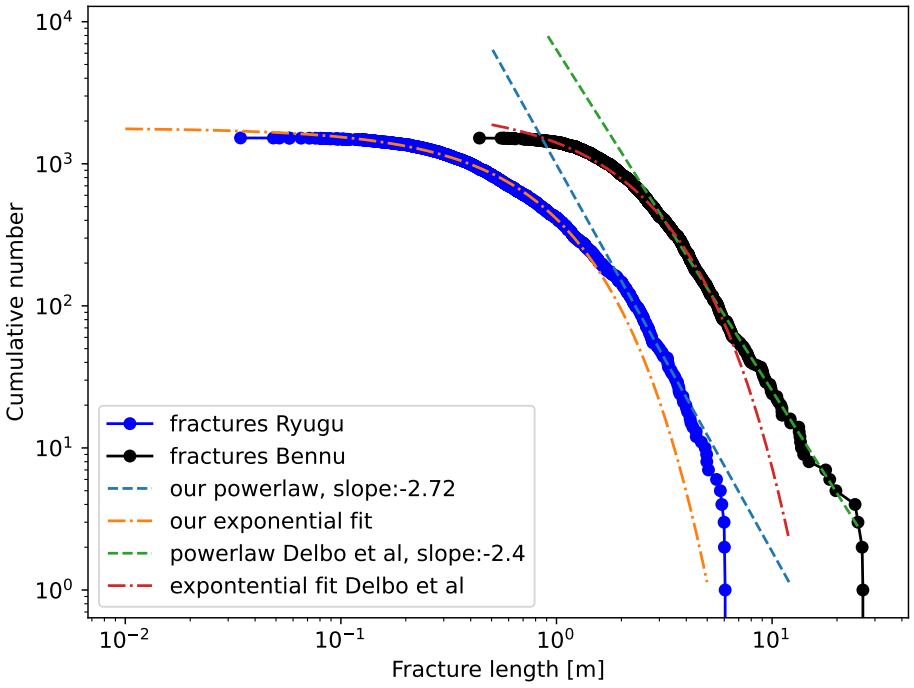

Figure 20.: Cumulative distribution of the length of fractures, the black curve is from Delbo et al. (2022), the blue curve is from Group 3 on Ryugu. The dashed orange and blue lines are power-laws, fitted to the right part of the plot. The dash-dotted red and green lines are exponential laws, fitted to the left part of the curves.

4.3. Fracture Propagation Model

The fracture propagation model of Delbo et al. (2022) was used to model the fracture growth on Ryugu. In Fig. 21 the theoretical fracture growth after 10.000 years on Bennu is visible. The plot shows the fracture length versus their amount. Starting at a random micro-fracture distribution, based on Bennu and Ryugu boulder data the model calculates the expected fracture growth and resulting fracture length distribution after a set duration (see section 3.3 after equation 3.9). The green modelled curve has moved to slightly larger values compared to the blue initial micro fracture distribution (drawn from Bryson et al. (2018). The black and grey curves are the observed fracture length distribution of Bennu and Ryugu. Whereas the orange curve to the right is the observed boulder diameter size frequency distribution of Bennu, representing the maximum possible lengths of fractures.

To use this model for Ryugu the complete thermo-physical properties from table 4 were inserted and the initial fracture distribution was changed to data by Michikami et al. (2019) instead of DellaGiustina et al. (2020). Resulting in a different fracture length distribution, plotted in Fig. 23, showing that all of Ryugu's fractures grew to their maximum possible size in the last 10.000 years. That does not seem plausible, and is probably explained by errors in the model or thermo-physical parameters that do not represent Ryugu's average boulder's properties well (scale-dependence, the values measured on a millimeter large grain might not represent a meter-sized boulder well). Since the result of the model is so heavily influenced by the material parameters of Ryugu and Bennu and they are compositionally similar bodies (Kitazato et al. (2019) and Kaplan et al. (2021)), it seems prudent to pick similar properties for Ryugu and Bennu. The values best constrained that differ significantly are the rotation period of 7.636 h compared to 4.296 h on Bennu and the measured temperature difference of 97° compared to 70° on Bennu.

When using these two values and otherwise identical parameters to Delbo et al. (2022) the obtained length distribution in Fig. 22 looks more realistic. Suggesting that the larger temperature variations on Ryugu accelerate fracture growth compared to Bennu. For this case the model computes that a thermal fracture that needs

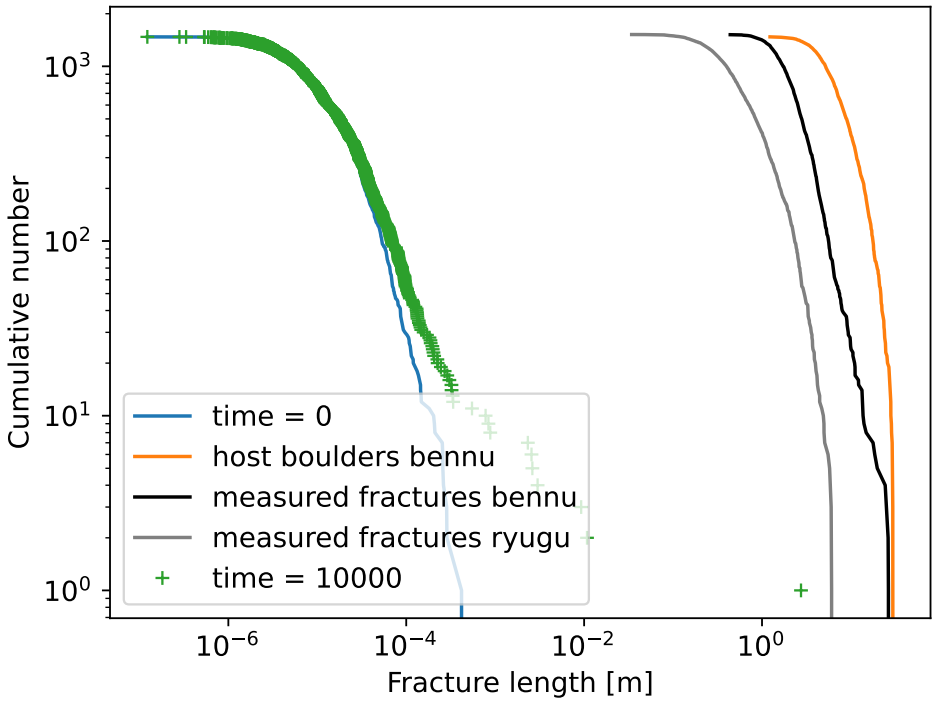

Figure 21.: Modelling of the evolution of a length distribution of fractures, here Bennu is modelled, exactly as in Delbo et al. (2022).
The blue curve is the initial random distribution of microscopic fractures at time 0. The green curve is the modelled fracture distribution after 10.000 years. Gray and black curves are the mapped fracture distributions of Ryugu and Bennu. The orange curve represents the maximum possible value, that is the diameter distribution of boulders on Bennu/Ryugu.

47.000 years to grow to a length of 3 meters on Bennu, would grow to this length in about 26.000 years on Ryugu. Which, with the observed fracture distribution on Ryugu, seen in Fig. 19, would suggest that the surface of Ryugu is even younger than the 40.000 year old surface of Bennu, as dated by Delbo et al. (2022).

To examine the influence of the chosen parameters, Bennu was again modelled in Fig. 24 with Bennu's temperature difference and rotation period, but with Ryugu's thermo-physical parameters from table 4. The distribution is again very close to the maximum achievable values based on the boulder sizes on Bennu after 10.000 years, suggesting that the model does not describe the complex processes of fracture formation adequately or the measured values of the returned samples do not represent the average boulder material on Ryugu well. This is further discussed in section 5.3

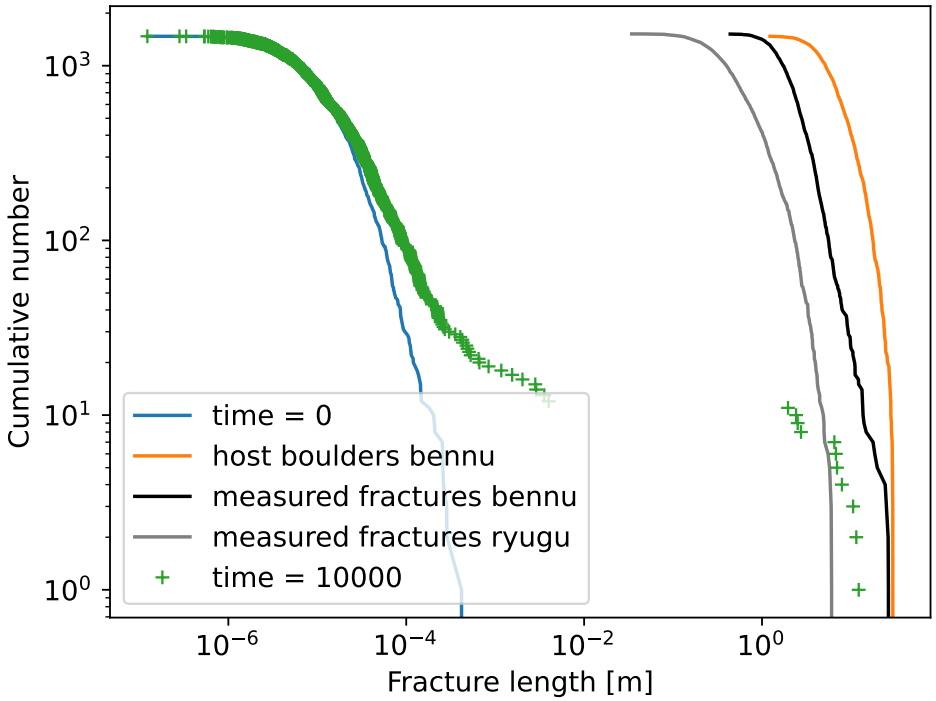

Figure 22.: Modelling of the evolution of a length distribution of fractures, here Ryugu is modelled, with Ryugu's temperature difference and period from table 4. The blue curve is the initial random distribution of microscopic fractures at time 0. The green curve is the modelled fracture distribution after 10.000 years. Gray and black curves are the mapped fracture distributions of Ryugu and Bennu. The orange curve represents the maximum possible value, that is the diameter distribution of boulders on Bennu/Ryugu.

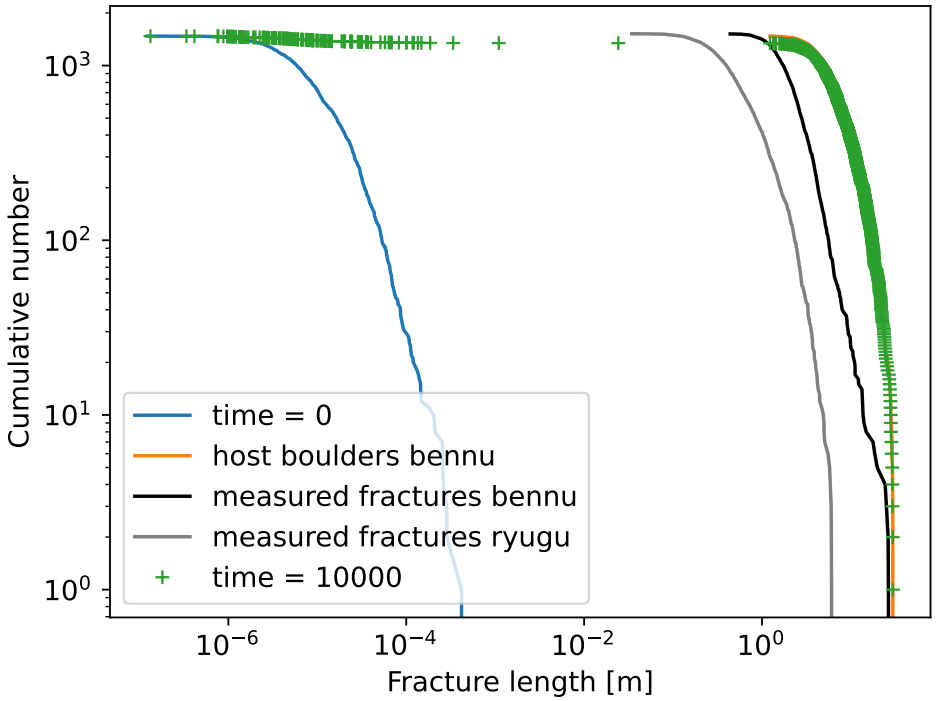

Figure 23.: Modelling of the evolution of a length distribution of fractures, here Ryugu is modelled, with all of Ryugus measured parameters from table 4. The green modelled curve reaches the maximum values possible after less than the modelled 10.000 years, this is not physically plausible and model error seems likely.
The blue curve is the initial random distribution of microscopic fractures at time 0. The green curve is the modelled fracture distribution after 10.000 years. Gray and black curves are the mapped fracture distributions of Ryugu and Bennu. The orange curve represents the maximum possible value, that is the diameter distribution of boulders on Bennu/Ryugu.

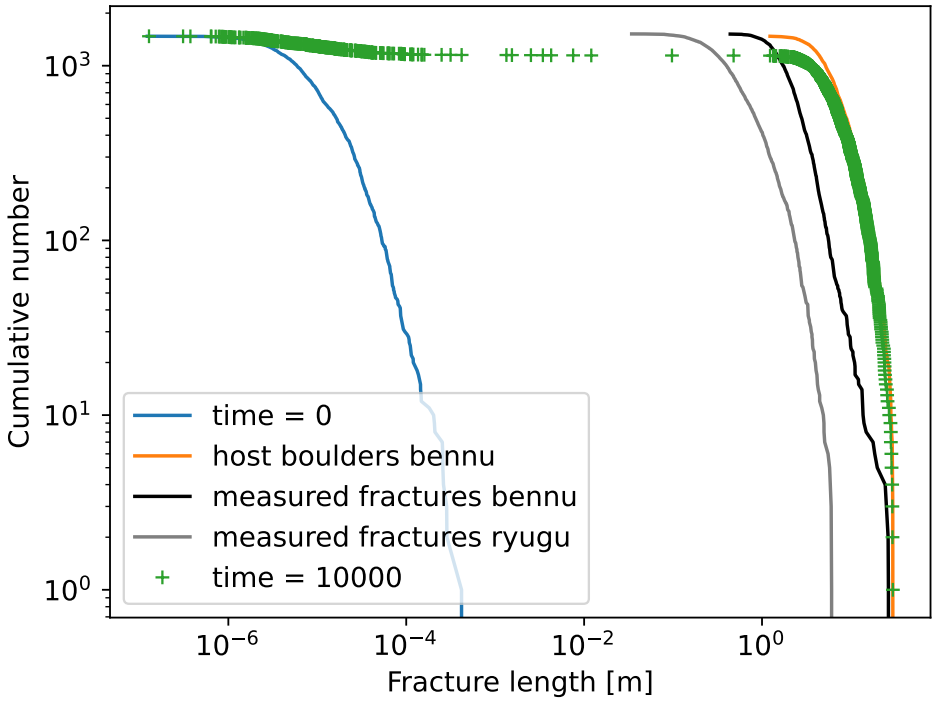

Figure 24.: Modelling of the evolution of a length distribution of fractures, here Bennu is modelled, with Ryugus thermophysical parameters from table 4.
The blue curve is the initial random distribution of microscopic fractures at time 0. The green curve is the modelled fracture distribution after 10.000 years. Gray and black curves are the mapped fracture distributions of Ryugu and Bennu. The orange curve represents the maximum possible value, that is the diameter distribution of boulders on Bennu/Ryugu.

5. Discussion

5.1. Fracture Orientation

The fractures in group one and two do not have a unambiguous preferred orientation, while group three does. This is interesting since the fractures in group three are often mapped close to the resolution limit making the identification of fractures more challenging. It is possible that the number of mapped fractures in group 1 (46) and group 2 (128) is not representative of the entirety of the fractures.

The strong North-South preference in fracture orientation of group 3 in Figure 18 is strong evidence for a thermal origin of these fractures: The eastern side of the observed boulders heats up in the morning, the western side in the evening, therefore fractures form orthogonal to the main stress axis. This is also a reported phenomenon on Earth (Eppes et al., 2015) and Mars (McFadden et al., 2005).

However, there are some problems with this: Shadows cast by small ridges and edges or overhangs and layers could be mistaken for fractures. Shadows are most prominent when the Sun is low and shines directly from West or East, so this could be another reason for the observed north-south orientation: the north-south fractures may just have better visibility. Delbo et al. (2022) discuss this for Bennu, but claim that, since fractures are identified at different latitudes, it can not be a strong influence. Importantly, Hayabusa2 typically observed the surface from the direction of the Sun (rather than orbiting its target like OSIRIS-REx), resulting in low phase angle data and narrow shadow width, which should minimize this problem.

It is also possible that due to limited image resolution some ridges or edges in the boulders could be mistaken for fractures, see Fig. 25. However ridges or edges in rocks are also part of the weathering of the rock, similar to fractures. In the unlikely worst case that all of the mapped features are in reality only ridges and edges, not

fractures, this would still lead to the conclusion that weathering on Ryugu somehow shows a preferred north-south orientation. Which then could also be explained by the thermal influence via sunlight at morning/evening.

Another source of error could be confirmation or selection bias, since I was aware of the results from Delbo et al. (2022). This could be prevented by a mapping setup where the author does not know the north direction, which would eliminate the possibility of the author selecting features that confirm the working hypotheses. Furthermore the study could also be improved via mapping done by multiple, independent authors that can confirm the validity of their results. Nevertheless, by reminding myself of these issues during the mapping process, I tried to avoid any bias.

It is also worth noting that this work found a clear North-South direction for Ryugus fractures, whereas Delbo et al. (2022) found a North-West South-East direction for Bennu's fractures. They discuss that this could be due to changes in Bennu's orbit in the last ten-thousands of years, which would imply that Ryugus orbit was more stable in the recent past. Okazaki et al. (2023) confirms this with an age of five million years for Ryugus current orbit.

The observed length distribution in Fig. 19 is very similar to the one Delbo et al. (2022) found for Bennu, suggesting that whatever previously discussed biases or errors may be present, the mapped features still result in a length distribution that is typical for fractures in boulders.

5.2. Length Distribution

Overall the compared length distributions of fractures in boulders on Ryugu and Bennu in Fig. 20 are quite similar, implying that the underlying formation mechanisms are similar. This is not surprising since Bennu and Ryugu are rather similar too. The observed fractures on Ryugu are smaller than on Bennu, which could be explained by the higher resolution of the Hayabusa2 Ryugu images compared to the mosaic used to study Bennu. This is probably also the reason why a comparable amount of fractures was observed in both studies, even though the Ryugu

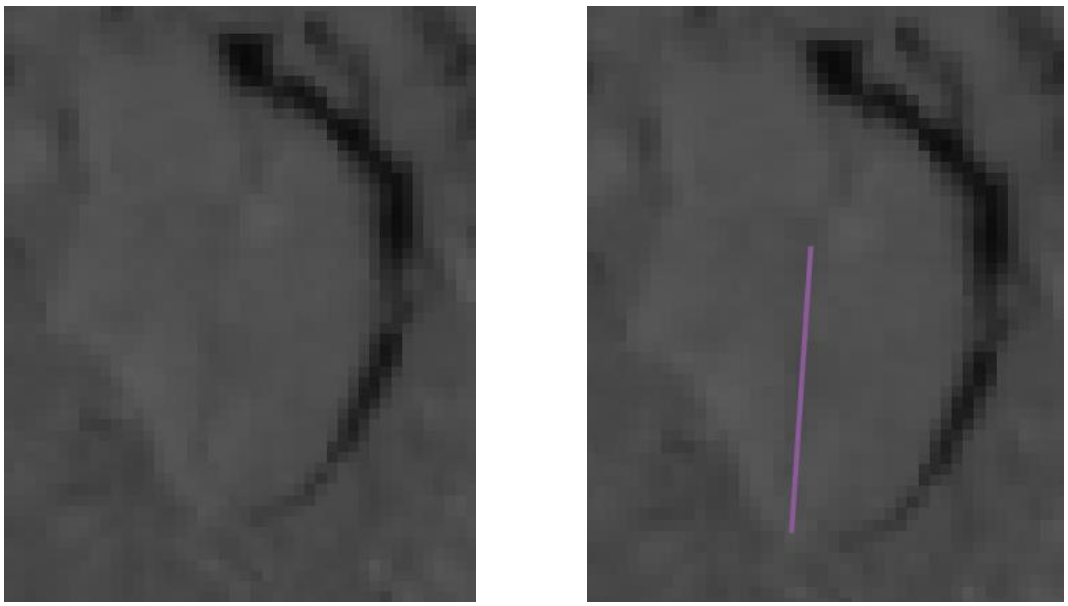

Figure 25.: Mapped features at resolution limit. Likely a fracture, but maybe also a ridge or edge?

data set was not global. Michikami et al. (2019) complements this, by observing more boulders on Ryugu than DellaGiustina et al. (2020) did on Bennu, allowing for more fractures in boulders to exist on Ryugu. Which is not surprising, since Ryugu is much larger than Bennu. Another explanation for smaller fractures on Ryugu could be a different composition to Bennu.

The fracture length distribution on Bennu as well as Ryugu is best described with a exponential law for fractures below about 3 to 4 meters, as seen in Fig. 20. Exponential laws have been used before to describe thermal induced fractures (Attree et al., 2018) and (Matonti et al., 2019). This exponential law then gets cut by a power-law, since fractures in boulders cannot grow without limit, they can only ever be as big as their host-boulder. Therefore the fracture length distribution above a certain size can be described with the same power-law that describes the boulder diameter.

5.3. Fracture Propagation Model

As visible in Fig. 23 the values for Ryugu's material properties in table 4 do not lead to reasonable results. Especially the material values from Nakamura et al. (2023) for Young's modulus and thermal expansion coefficient cause the model to accelerate

the fracture growth to values larger than physically possible.

This might be because the measured values were obtained from a millimeter sized grain in a terrestrial lab. Whereas the values used by Delbo et al. (2022) are estimated bulk values, that may describe the modelled objects better. As they produce reasonable results in Figs. 21 and 22. An explanation for this could be that the measured values by Nakamura et al. (2023) do not take into account the porosity and morphology of the boulders.

Because these material values come with large uncertainties and to make a comparison of fracture formation on Bennu and Ryugu feasible, it seems prudent to use identical values for Bennu's and Ryugu's heat capacity, density, thermal inertia, thermal expansion coefficient, Poisson ratio and Young's modulus. Leading to only the values that are well constrained and influence the fracture formation being changed (temperature difference, rotational period). As was done in Fig. 22. This allows to estimate the timescale on which thermal fracturing takes place on Bennu and Ryugu, in this case slightly shorter timescales as reported by Delbo et al. (2022) (approx. 40.000 years) are calculated for Ryugu.

However, the dubious output of the model in Fig. 23 with real, measured parameters by Nakamura et al. (2023) for Ryugu also calls the reported timescale of 40.000 years by Delbo et al. (2022) into question: if measured material properties produce physically unrealistic output, the confidence in the same modelling done with estimated parameters is questionable at best.

5.4. Sensitivity Analysis

To further analyse which parameter has what influence on the resulting fracture growth a sensitivity analysis was done. For this each of the parameters listed in table 4 was varied and it was measured how much time was needed to grow a 10 m long fracture. After this the boulder is broken and the fracture can not grow anymore, as visible in Fig. 15 in chapter 3.

Seven of the analysed parameters are positively correlated with the fracture growth speed, meaning a higher value leads to a shorter fracturing time of the 10 m long

boulder. Among them are Paris Law pre-factor C, density ρ, heat capacity C_p, thermal expansion coefficient α, Poisson ratio ν, Young's Modulus E and the temperature difference ΔT. Visible in Figs. 26 to 32.

Three of the parameters are negatively correlated with the fracture growth speed. Meaning higher values lead to larger fracturing times. Those are Paris' Law Exponent n, thermal inertia Γ and rotation Period P. Visible in Figs. 33, 34 and 35. Notably P is the only dependency that looks like it grows linearly. Also, in reality a increase of Period P would lead to an increase of the temperature difference $d\Delta T$, which is not the case in this sensitivity analyses, therefore Fig. 35 is not really realistic.

Interestingly Delbo et al. (2014) observe linear graphs for Paris' Law pre-factor C and exponent n dependency, whereas I obtain nonlinear curves in Figs. 26 and 33.

To quantify the influence of the discussed parameters a first order sensitivity index S_i after Saltelli et al. (2007) was calculated:

$$S_i = \left| \frac{\Delta y}{\Delta x} \right| \tag{5.1}$$

Where y is the model output parameter, so in this case the needed fracturing time, to split a 10 m long boulder and x is the specific parameter, listed in table 7.

The obtained indices help to explain the results of the model in section 4.3. The parameter with the largest influence on the output is the thermal expansion coefficient α, this is also the parameter in tables 3 and 4 with quite a big discrepancy between Delbo et al. (2022) and the measured values by Nakamura et al. (2023). This leads to the questionable results in Figs. 23 and 24.

C, n and ν also have large Sensitivity Index values in table 7, but were not changed in the modelling of Ryugu and Bennu, and therefore have no effect on the results there. Rotation period P also has quite a big value for the Sensitivity Index, but in reality is not independent of temperature difference ΔT. Young's modulus E also has a sizeable Sensitivity Index and the values in table 4 also differ by almost 50 %. But since the used value is smaller than the one used by Delbo et al. (2022), it somewhat helps to mitigate the large effect caused by the change in α. Interestingly

Parameter	Sensitivity Index S_i
α	1.55×10^9
C	5.92×10^7
ν	1.41×10^5
n	6.73×10^4
P	1.32×10^4
E	3.84×10^3
ΔT	9.44×10^2
Γ	2.35×10^1
ρ	6.7×10^0
C_p	5×10^0

Table 7.: Sensitivity Indices for the analysed parameters. Note that the unit of these is $year/unit$, in which unit is the unit of the specific parameter.

the influence of Thermal Inertia Γ, density ρ and heat capacity C_p seems to be quite small.

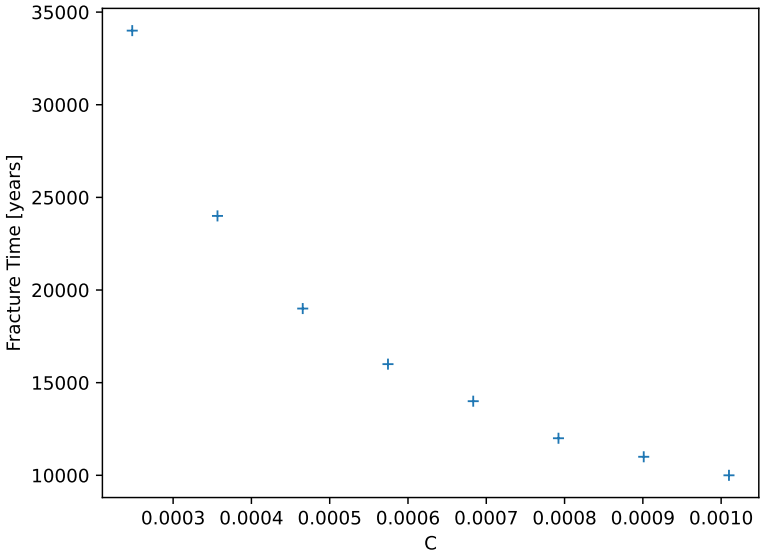

Figure 26.: Sensitivity of the fracturing time of a 10 m long boulder to variations in Paris' Law pre-factor C. Paris' Law pre-factor is dimensionless. Larger values lead to faster fracture growth.

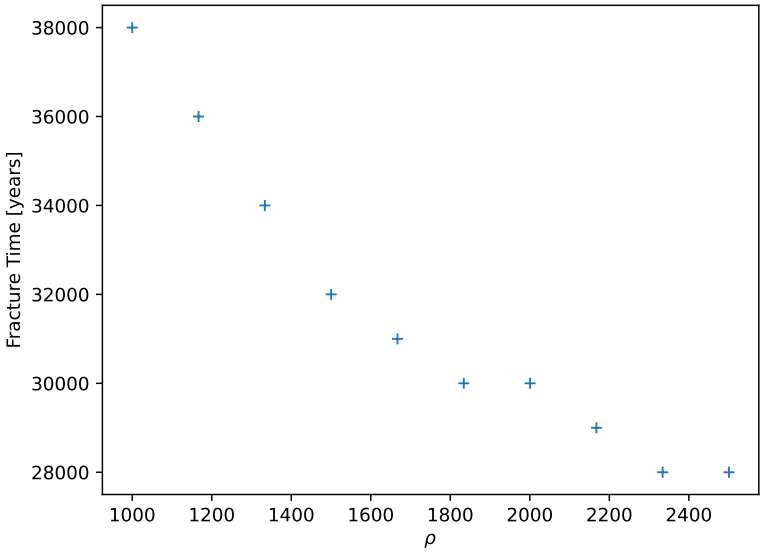

Figure 27.: Sensitivity of the fracturing time of a 10 m long boulder to variations in density ρ. The unit of ρ is kg/m^{-3}. Larger values lead to faster fracture growth.

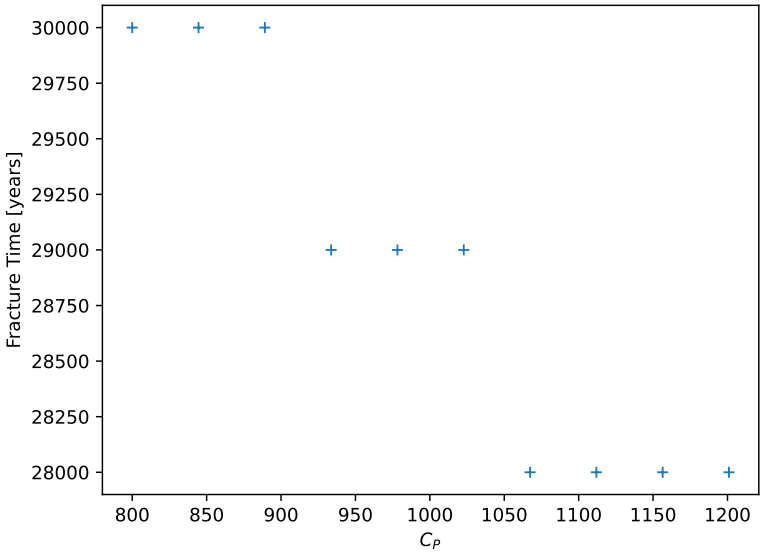

Figure 28.: Sensitivity of the fracturing time of a 10 m long boulder to variations in heat capacity C_p. The unit of C_p is $J * kg^{-1} * K^{-1}$. Larger values lead to faster fracture growth.

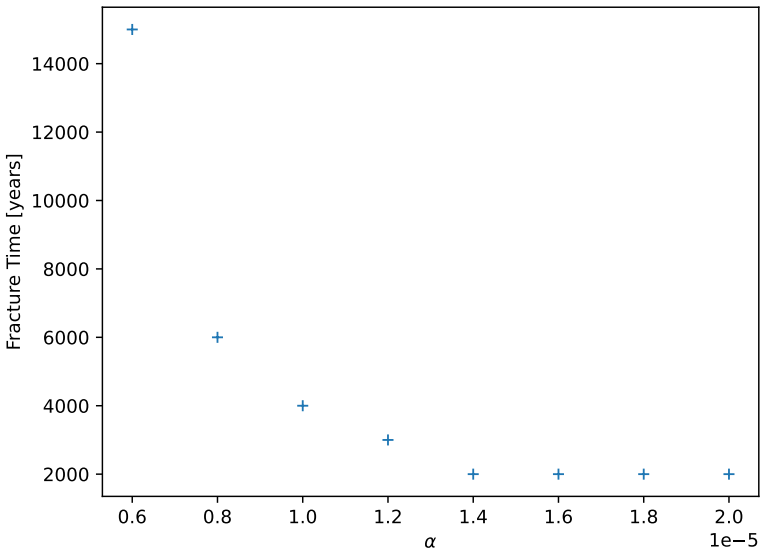

Figure 29.: Sensitivity of the fracturing time of a 10 m long boulder to variations in thermal expansion coefficient α. The unit of α is K^{-1}. Larger values lead to faster fracture growth.

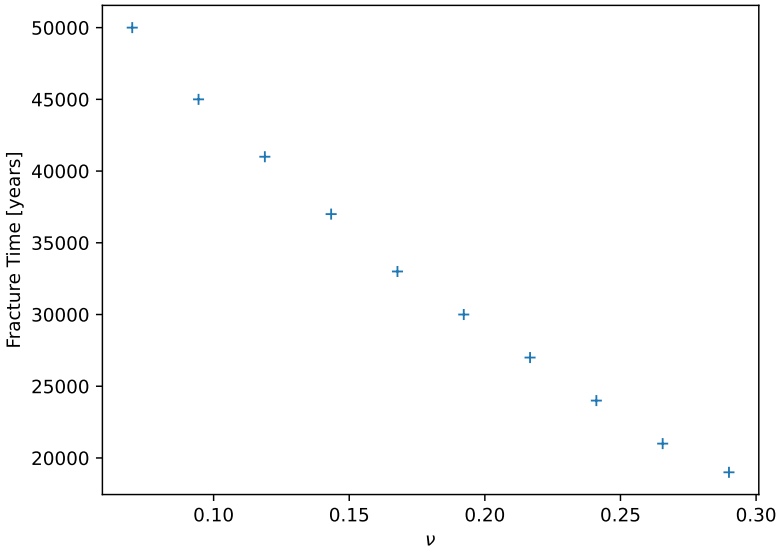

Figure 30.: Sensitivity of the fracturing time of a 10 m long boulder to variations in Poisson Ratio ν. ν is dimensionless. Larger values lead to faster fracture growth.

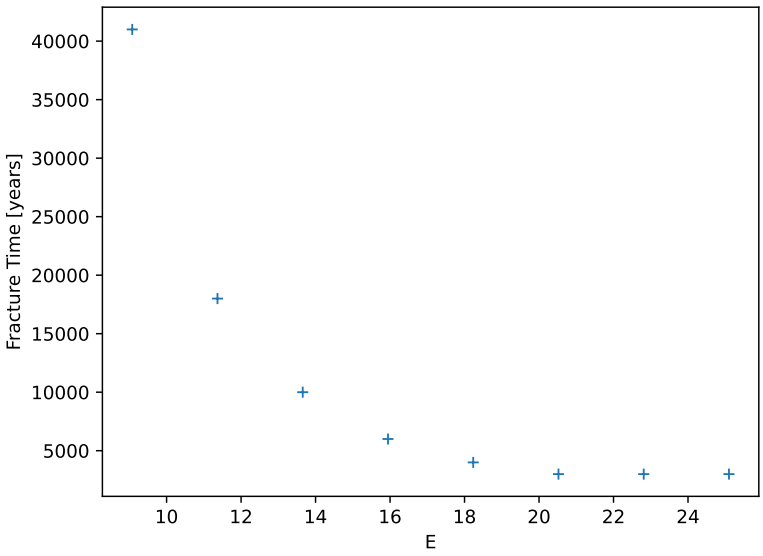

Figure 31.: Sensitivity of the fracturing time of a 10 m long boulder to variations in Young's Modulus E. The unit of E is GPa. Larger values lead to faster fracture growth.

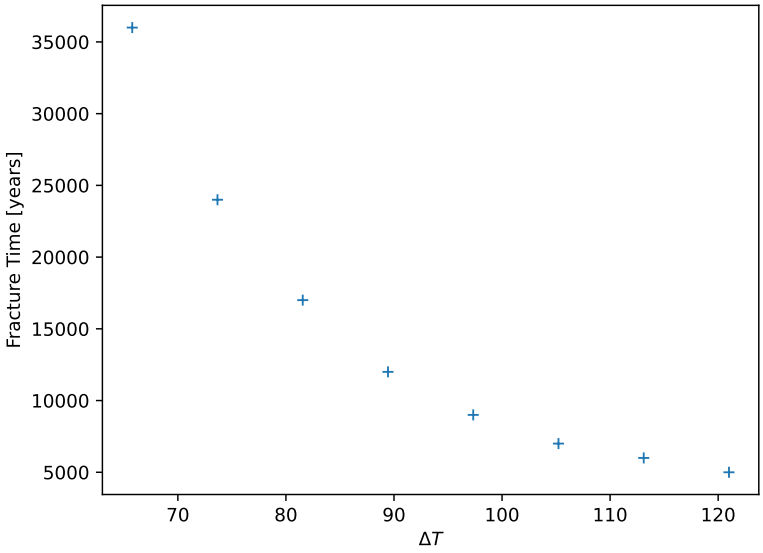

Figure 32.: Sensitivity of the fracturing time of a 10 m long boulder to variations in temperature difference ΔT. The unit of ΔT is K. Larger values lead to faster fracture growth.

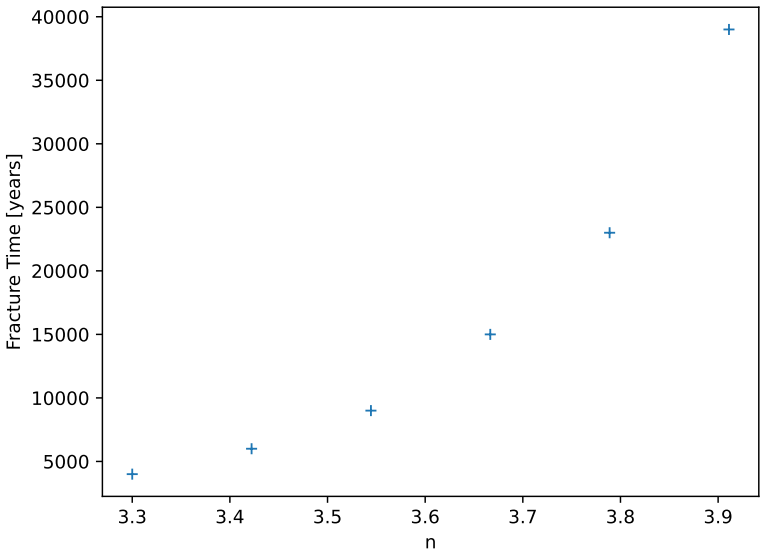

Figure 33.: Sensitivity of the fracturing time of a 10 m long boulder to variations in Paris Law exponent n. n is dimensionless. Larger values lead to slower fracture growth.

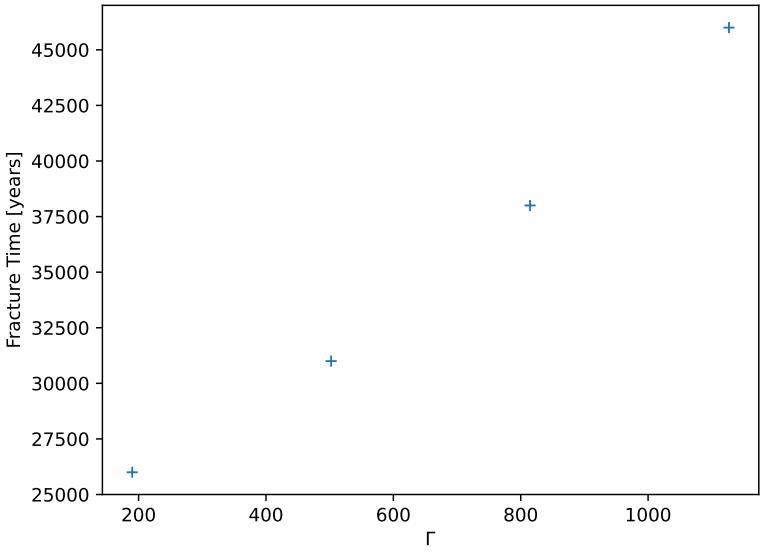

Figure 34.: Sensitivity of the fracturing time of a 10 m long boulder to variations in Thermal Inertia Γ. The unit of Γ is $J * m^{-2} * K^{-1} * s^{-0.5}$. Larger values lead to slower fracture growth.

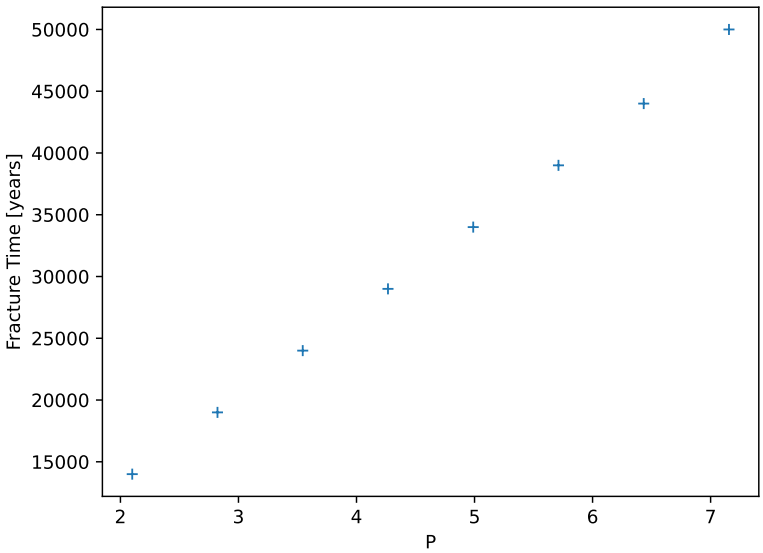

Figure 35.: Sensitivity of the fracturing time of a 10 m long boulder to variations in rotational period P. The unit of P is hours. Larger values lead to slower fracture growth.

6. Conclusion

Delbo et al. (2022) mapped fractures on a global mosaic of Near-Earth-Asteroid Bennu, analyzing their length distribution and orientation. Through this a thermal origin for the fractures was found. Furthermore the fracture length distribution was used to model fracture growth, allowing to constrain the time-scale on which thermal fracturing takes place.

I repeated this work, but instead of a global mosaic of Bennu, I used selected high-resolution images of Ryugu as underlying data. The fractures on Ryugu's boulders show a strong north-south orientation. This is probably due to thermal stress, where the largest temperature gradient is oriented east-west. The observed fracture length distribution for Ryugu is similar to the one found on Bennu and fits a exponential law, similar to other thermal induced fractures (Attree et al. (2018) and Matonti et al. (2019)), further suggesting a thermal origin for Ryugu's fractures. This is also strong evidence for the validity of the mapping: whatever biases and errors may be present, they could not have a strong impact, otherwise a different length distribution would be found.

The fracture propagation model by Delbo et al. (2022) was adapted for use on Ryugu. The results suggest a similar timescale for thermal fracturing on Ryugu's surface to Bennu's when using the same thermo-physical parameters and only adjusting the rotation period and surface temperature.

However the dubious results (see Fig. 23) with measured material parameters by Nakamura et al. (2023) potentially also cast doubt on the validity of Delbo et al. (2022) timescale determination, because their model does not produce reasonable results with real material properties.

The sensitivity analysis in 5.4 shows that most of the result can be explained by the change in thermal expansion coefficient α in table 4 found by Nakamura et al.

(2023) for Ryugu's material.

7. Outlook

7.1. Further candidates

To further validate the discovered fracture orientation, length distribution and the propagation model, it would be interesting to repeat the work done here for another small body. This could confirm the findings on Bennu and Ryugu and in that case, would suggest that north-south oriented fractures on small bodies under the sun's illumination influence follow are a regular phenomenon. Appropriate candidates with high resolution images available could potentially be the comet 67P with the images by the Rosetta Mission or maybe the asteroid Didymos, which will be visited by the Hera Mission, although these two bodies are different in composition and structure.

7.2. Automation

It might be a good idea to dedicate resources to the development of a tool that automates fracture detection in images. Obviously machine learning and neural networks have gathered a lot of scientific interest in the recent past, but even traditional image processing methods like filters or edge detection could lead to a huge increase in fracture data acquisition, resulting in even more evidence for (or against) thermal fracturing on small bodies and is independent of the subjective mapping process when conducted by scientists.

Bibliography

Ajluni, T., Everett, D., Linn, T., Mink, R., Willcockson, W., & Wood, J. (2015). Osiris-rex, returning the asteroid sample. In *2015 ieee aerospace conference* (p. 1-15). doi: 10.1109/AERO.2015.7118988

Andrews, D. G., Bonner, K., Butterworth, A., Calvert, H., Dagang, B., Dimond, K., … others (2015). Defining a successful commercial asteroid mining program. *Acta Astronautica*, *108*, 106–118.

Attree, N., Groussin, O., Jorda, L., Rodionov, S., Auger, A.-T., Thomas, N., … Hartogh, P. (2018, February). Thermal fracturing on comets. *Astronomy and Astrophysics*, *610*, A76. Retrieved from https://doi.org/10.1051/0004-6361/201731937 doi: 10.1051/0004-6361/201731937

Bennett, C., DellaGiustina, D., Becker, K., Becker, T., Edmundson, K., Golish, D., … Lauretta, D. (2021). A high-resolution global basemap of (101955) bennu. *Icarus*, *357*, 113690. Retrieved from https://www.sciencedirect.com/science/article/pii/S0019103520300816 doi: https://doi.org/10.1016/j.icarus.2020.113690

Bottke, W. F., Durda, D. D., Nesvorný, D., Jedicke, R., Morbidelli, A., Vokrouhlický, D., & Levison, H. (2005). The fossilized size distribution of the main asteroid belt. *Icarus*, *175*(1), 111-140. Retrieved from https://www.sciencedirect.com/science/article/pii/S0019103504003811 doi: https://doi.org/10.1016/j.icarus.2004.10.026

Bryson, K. L., Ostrowski, D. R., & Blasizzo, A. (2018, December). Meteorite flaws and scaling for atmospheric entry. *Planetary and Space Science*, *164*, 85–90. Retrieved from https://doi.org/10.1016/j.pss.2018.06.018 doi: 10.1016/j.pss.2018.06.018

Cartwright, D. J., & Rooke, D. P. (1975, October). Evaluation of stress intensity factors. *Journal of Strain Analysis*, *10*(4), 217–224. Retrieved from https://doi.org/10.1243/03093247v104217 doi: 10.1243/03093247v104217

Delbo, M., Libourel, G., Wilkerson, J., Murdoch, N., Michel, P., Ramesh, K. T., … Marchi, S. (2014, April). Thermal fatigue as the origin of regolith on small asteroids. *Nature*, *508*(7495), 233–236. Retrieved from https://doi.org/10.1038/nature13153 doi: 10.1038/nature13153

Delbo, M., Walsh, K. J., Matonti, C., Wilkerson, J., Pajola, M., Al Asad, M. M., … others (2022). Alignment of fractures on bennu's boulders indicative of rapid asteroid surface evolution. *Nature Geoscience*, *15*(6), 453–457.

DellaGiustina, D. N., Burke, K. N., Walsh, K. J., Smith, P. H., Golish, D. R., Bierhaus, E. B., … Lauretta, D. S. (2020, November). Variations in color and reflectance on the surface of asteroid (101955) bennu. *Science*, *370*(6517). Retrieved from https://doi.org/10.1126/science.abc3660 doi: 10.1126/science.abc3660

El Mir, C., Ramesh, K., & Delbo, M. (2019). The efficiency of thermal fatigue in regolith generation on small airless bodies. *Icarus*, *333*, 356-370. Retrieved from https://www.sciencedirect.com/science/article/pii/S0019103518307048 doi: https://doi.org/10.1016/j.icarus.2019.06.001

Eppes, M.-C., Willis, A., Molaro, J., Abernathy, S., & Zhou, B. (2015, Mar). *Cracks in martian boulders exhibit preferred orientations that point to solar-induced thermal stress.* Nature Publishing Group. Retrieved from https://www.nature.com/articles/ncomms7712#citeas

Grott, M., Knollenberg, J., Hamm, M., Ogawa, K., Jaumann, R., Otto, K. A., … Moussi-Soffys, A. (2019, July). Low thermal conductivity boulder with high porosity identified on c-type asteroid (162173) ryugu. *Nature Astronomy*, *3*(11), 971–976. Retrieved from https://doi.org/10.1038/s41550-019-0832-x doi: 10.1038/s41550-019-0832-x

Ho, T.-M., Jaumann, R., Bibring, J.-P., Grott, M., Glaßmeier, K.-H., Moussi, A., … others (2021). The mascot lander aboard hayabusa2: the in-situ exploration of nea (162173) ryugu. *Planetary and Space Science*, *200*, 105200.

Johansen, A., Low, M.-M. M., Lacerda, P., & Bizzarro, M. (2015). Growth of asteroids, planetary embryos, and kuiper belt objects by chondrule accretion. *Science Advances*, *1*(3), e1500109.

Kameda, S., Suzuki, H., Takamatsu, T., Cho, Y., Yasuda, T., Yamada, M., … Sugita, S. (2016, May). Preflight calibration test results for optical navigation camera telescope (ONC-t) onboard the hayabusa2 spacecraft. *Space Science Reviews*, *208*(1-4), 17–31. Retrieved from https://doi.org/10.1007/s11214-015-0227-y doi: 10.1007/s11214-015-0227-y

Kaplan, H. H., Simon, A. A., Hamilton, V. E., Thompson, M. S., Sandford, S. A., Barucci, M. A., … Lauretta, D. S. (2021, September). Composition of organics on asteroid (101955) bennu. *Astronomy and Astrophysics*, *653*, L1. Retrieved

from https://doi.org/10.1051/0004-6361/202141167 doi: 10.1051/0004-6361/202141167

Kitazato, K., Milliken, R. E., Iwata, T., Abe, M., Ohtake, M., Matsuura, S., … Tsuda, Y. (2019, April). The surface composition of asteroid 162173 ryugu from hayabusa2 near-infrared spectroscopy. *Science*, *364*(6437), 272–275. Retrieved from https://doi.org/10.1126/science.aav7432 doi: 10.1126/science.aav7432

Lauretta, D. S., Balram-Knutson, S. S., Beshore, E., Boynton, W. V., d'Aubigny, C. D., DellaGiustina, D. N., … Sandford, S. A. (2017, August). OSIRIS-REx: Sample return from asteroid (101955) bennu. *Space Science Reviews*, *212*(1-2), 925–984. Retrieved from https://doi.org/10.1007/s11214-017-0405-1 doi: 10.1007/s11214-017-0405-1

Lauretta, D. S., DellaGiustina, D. N., Bennett, C. A., Golish, D. R., Becker, K. J., Balram-Knutson, S. S., … Wolner, C. W. V. (2019, March). The unexpected surface of asteroid (101955) bennu. *Nature*, *568*(7750), 55–60. Retrieved from https://doi.org/10.1038/s41586-019-1033-6 doi: 10.1038/s41586-019-1033-6

Lauretta, D. S., Enos, H. L., Polit, A. T., Roper, H. L., & Wolner, C. W. (2021). Chapter 8 - osiris-rex at bennu: Overcoming challenges to collect a sample of the early solar system. In A. Longobardo (Ed.), *Sample return missions* (p. 163-194). Elsevier. Retrieved from https://www.sciencedirect.com/science/article/pii/B9780128183304000082 doi: https://doi.org/10.1016/B978-0-12-818330-4.00008-2

Longley, P. A., Goodchild, M. F., Maguire, D. J., & Rhind, D. W. (2005). *Geographic information systems and science* (2nd ed.). Chichester, England: John Wiley & Sons.

Matonti, C., Attree, N., Groussin, O., Jorda, L., Viseur, S., Hviid, S. F., … Vincent, J.-B. (2019, February). Bilobate comet morphology and internal structure controlled by shear deformation. *Nature Geoscience*, *12*(3), 157–162. Retrieved from https://doi.org/10.1038/s41561-019-0307-9 doi: 10.1038/s41561-019-0307-9

McFadden, L., Eppes, M., Gillespie, A., & Hallet, B. (2005, 01). Physical weathering in arid landscapes due to diurnal variation in the direction of solar heating. *GSA Bulletin*, *117*(1-2), 161-173. Retrieved from https://doi.org/10.1130/B25508.1 doi: 10.1130/B25508.1

Michel, P., Benz, W., Tanga, P., & Richardson, D. C. (2001). Collisions and gravitational reaccumulation: Forming asteroid families and satellites. *Science*, *294*(5547), 1696-1700. Retrieved from https://www.science.org/doi/abs/10.1126/science.1065189 doi: 10.1126/science.1065189

Michikami, T., Honda, C., Miyamoto, H., Hirabayashi, M., Hagermann, A., Irie, T., … Sugita, S. (2019, October). Boulder size and shape distributions on asteroid ryugu. *Icarus*, *331*, 179–191. Retrieved from https://doi.org/10.1016/j.icarus.2019.05.019 doi: 10.1016/j.icarus.2019.05.019

Nakamura, T., Matsumoto, M., Amano, K., Enokido, Y., Zolensky, M. E., Mikouchi, T., … Tsuda, Y. (2023). Formation and evolution of carbonaceous asteroid ryugu: Direct evidence from returned samples. *Science*, *379*(6634), eabn8671. Retrieved from https://www.science.org/doi/abs/10.1126/science.abn8671 doi: 10.1126/science.abn8671

NASA Navigation Ancillary Information Facility. (2023). Spice toolkit [Computer software manual]. Retrieved from https://naif.jpl.nasa.gov/naif/toolkit.html

NZZ. (2020). *Berner forscher lüftet rätsel um diamantähnliche asteroiden.* Retrieved 2023-06-30, from https://www.nzz.ch/wissenschaft/asteroiden-bennu-und-ryugu-schweizer-forscher-erklaert-skurrile-form-ld.1559440

Okazaki, R., Marty, B., Busemann, H., Hashizume, K., Gilmour, J. D., Meshik, A., … Tsuda, Y. (2023). Noble gases and nitrogen in samples of asteroid ryugu record its volatile sources and recent surface evolution. *Science*, *379*(6634), eabo0431. Retrieved from https://www.science.org/doi/abs/10.1126/science.abo0431 doi: 10.1126/science.abo0431

Paris, P. C. (1961). A rational analytic theory of fatigue. *Trends Engineering*, *13*, 9–14.

QGIS Development Team. (2023). Qgis geographic information system [Computer software manual]. Retrieved from http://qgis.org

Ravaji, B., Alí-Lagoa, V., Delbo, M., & Wilkerson, J. W. (2019, December). Unraveling the mechanics of thermal stress weathering: Rate-effects, size-effects, and scaling laws. *Journal of Geophysical Research: Planets*, *124*(12), 3304–3328. Retrieved from https://doi.org/10.1029/2019je006019 doi: 10.1029/2019je006019

Rie, H., Manabu, Y., M. Katherine, C., Yukio, Y., Shin-ya, M., Toru, K., … Seiji, S. (2022). *Software interface specification for the hayabusa2 optical navigation camera (onc) data products.* Retrieved 2023-06-29, from https://sbnarchive.psi.edu/pds4/hayabusa2/certified/hyb2_onc/document/hyb2_onc_dpsis.pdf

Saiki, T., Sawada, H., Okamoto, C., Yano, H., Takagi, Y., Akahoshi, Y., & Yoshikawa, M. (2013). Small carry-on impactor of hayabusa2 mission. *Acta Astronautica*, *84*, 227-236. Retrieved from https://www.sciencedirect.com/science/article/pii/S0094576512004614 doi: https://doi.org/10.1016/j.actaastro.2012.11.010

Sakatani, N., Tanaka, S., Okada, T., Fukuhara, T., Riu, L., Sugita, S., ... Tsuda, Y. (2021, May). Anomalously porous boulders on (162173) ryugu as primordial materials from its parent body. *Nature Astronomy*, *5*(8), 766–774. Retrieved from https://doi.org/10.1038/s41550-021-01371-7 doi: 10.1038/s41550-021-01371-7

Saltelli, A., Ratto, M., Andres, T., Campolongo, F., Cariboni, J., Gatelli, D., ... Tarantola, S. (2007). *Global sensitivity analysis. the primer*. Wiley. Retrieved from https://doi.org/10.1002/9780470725184 doi: 10.1002/9780470725184

Sugita, S. (2022). *Hayabusa2 optical navigation camera (onc)*. Retrieved 2022-10-26, from https://data.darts.isas.jaxa.jp/pub/hayabusa2/onc_bundle/browse/

Sugita, S., Honda, R., Morota, T., Kameda, S., Sawada, H., Tatsumi, E., ... Tsuda, Y. (2019). The geomorphology, color, and thermal properties of ryugu: Implications for parent-body processes. *Science*, *364*(6437), eaaw0422. Retrieved from https://www.science.org/doi/abs/10.1126/science.aaw0422 doi: 10.1126/science.aaw0422

Tsuda, Y., Yoshikawa, M., Abe, M., Minamino, H., & Nakazawa, S. (2013). System design of the hayabusa 2—asteroid sample return mission to 1999 ju3. *Acta Astronautica*, *91*, 356-362. Retrieved from https://www.sciencedirect.com/science/article/pii/S009457651300218X doi: https://doi.org/10.1016/j.actaastro.2013.06.028

Wada, K., Grott, M., Michel, P., Walsh, K. J., Barucci, A. M., Biele, J., ... others (2018). Asteroid ryugu before the hayabusa2 encounter. *Progress in Earth and Planetary Science*, *5*(1), 1–30.

Walsh, K. J. (2018, September). Rubble pile asteroids. *Annual Review of Astronomy and Astrophysics*, *56*(1), 593–624. Retrieved from https://doi.org/10.1146/annurev-astro-081817-052013 doi: 10.1146/annurev-astro-081817-052013

Watanabe, S., Hirabayashi, M., Hirata, N., Hirata, N., Noguchi, R., Shimaki, Y., ... Tsuda, Y. (2019). Hayabusa2 arrives at the carbonaceous asteroid 162173 ryugu;a spinning top shaped rubble pile. *Science*, *364*(6437), 268-272. Retrieved from

https://www.science.org/doi/abs/10.1126/science.aav8032 doi: 10.1126/science.aav8032

Watanabe, S.-i., Tsuda, Y., Yoshikawa, M., Tanaka, S., Saiki, T., & Nakazawa, S. (2017). Hayabusa2 mission overview. *Space Science Reviews*, *208*(1), 3–16.

A. Appendix

Listing 1: Used high-resolution Hayabusa2 images

```
'hyb2_onc_20180806_225848_tvf_l2d',
'hyb2_onc_20180921_025306_tvf_l2d',
'hyb2_onc_20180921_025442_tuf_l2d',
'hyb2_onc_20180921_033442_tvf_l2d',
'hyb2_onc_20180921_033618_tuf_l2d',
'hyb2_onc_20180921_034938_tvf_l2d',
'hyb2_onc_20180921_035114_tuf_l2d',
'hyb2_onc_20180921_040154_tvf_l2d',
'hyb2_onc_20180921_040402_tvf_l2d',
'hyb2_onc_20180921_040634_tvf_l2d',
'hyb2_onc_20180921_041826_tvf_l2d',
'hyb2_onc_20180921_042106_tvf_l2d',
'hyb2_onc_20180921_042418_tvf_l2d',
'hyb2_onc_20180921_042730_tvf_l2d',
'hyb2_onc_20180921_043010_tvf_l2d',
'hyb2_onc_20181003_003036_tvf_l2d',
'hyb2_onc_20181003_003212_tuf_l2d',
'hyb2_onc_20181003_012044_tvf_l2d',
'hyb2_onc_20181003_012220_tuf_l2d',
'hyb2_onc_20181003_013540_tvf_l2d',
'hyb2_onc_20181003_013553_twf_l2d',
'hyb2_onc_20181003_013716_tuf_l2d',
'hyb2_onc_20181003_014756_tvf_l2d',
'hyb2_onc_20181003_015004_tvf_l2d',
'hyb2_onc_20181003_015212_tvf_l2d',
'hyb2_onc_20181003_015420_tvf_l2d',
'hyb2_onc_20181003_015653_tvf_l2d',
'hyb2_onc_20181003_021156_tvf_l2d',
'hyb2_onc_20181003_021436_tvf_l2d',
'hyb2_onc_20181003_021748_tvf_l2d',
'hyb2_onc_20181003_022100_tvf_l2d',
'hyb2_onc_20181003_022340_tvf_l2d',
'hyb2_onc_20181003_022652_tvf_l2d',
'hyb2_onc_20181015_130717_twf_l2d',
'hyb2_onc_20181015_132213_twf_l2d',
'hyb2_onc_20181015_132337_tuf_l2d',
'hyb2_onc_20181015_133045_twf_l2d',
```

```
'hyb2_onc_20181015_133209_tuf_l2d',
'hyb2_onc_20181015_133625_tvf_l2d',
'hyb2_onc_20181015_133833_tvf_l2d',
'hyb2_onc_20181015_134041_tvf_l2d',
'hyb2_onc_20181015_134616_tvf_l2d',
'hyb2_onc_20181015_134627_twf_l2d',
'hyb2_onc_20181015_134638_txf_l2d',
'hyb2_onc_20181015_134655_tpf_l2d',
'hyb2_onc_20181015_134707_tbf_l2d',
'hyb2_onc_20181015_134718_tuf_l2d',
'hyb2_onc_20181015_134935_tvf_l2d',
'hyb2_onc_20181015_135038_tuf_l2d',
'hyb2_onc_20181015_135255_tvf_l2d',
'hyb2_onc_20181015_135358_tuf_l2d',
'hyb2_onc_20181015_140115_tvf_l2d',
'hyb2_onc_20181015_140218_tuf_l2d',
'hyb2_onc_20181025_015814_tuf_l2d',
'hyb2_onc_20181025_021134_tvf_l2d',
'hyb2_onc_20181025_021310_tuf_l2d',
'hyb2_onc_20181025_022006_tvf_l2d',
'hyb2_onc_20181025_022142_tuf_l2d',
'hyb2_onc_20181025_022558_tvf_l2d',
'hyb2_onc_20181025_022806_tvf_l2d',
'hyb2_onc_20181025_023014_tvf_l2d',
'hyb2_onc_20181025_030628_tuf_l2d',
'hyb2_onc_20190221_205818_tvf_l2d',
'hyb2_onc_20190221_205954_tuf_l2d',
'hyb2_onc_20190221_213610_tvf_l2d',
'hyb2_onc_20190221_213746_tuf_l2d',
'hyb2_onc_20190221_215106_tvf_l2d',
'hyb2_onc_20190221_215242_tuf_l2d',
'hyb2_onc_20190221_215938_tvf_l2d',
'hyb2_onc_20190221_220022_tnf_l2d',
'hyb2_onc_20190221_220114_tuf_l2d',
'hyb2_onc_20190221_220322_tvf_l2d',
'hyb2_onc_20190221_220530_tvf_l2d',
'hyb2_onc_20190308_021228_tvf_l2d',
'hyb2_onc_20190308_021404_tuf_l2d',
'hyb2_onc_20190308_025052_tvf_l2d',
'hyb2_onc_20190308_025228_tuf_l2d',
'hyb2_onc_20190308_030548_tvf_l2d',
'hyb2_onc_20190308_030724_tuf_l2d',
'hyb2_onc_20190308_031420_tvf_l2d',
'hyb2_onc_20190308_031504_tnf_l2d',
'hyb2_onc_20190308_031556_tuf_l2d',
'hyb2_onc_20190308_031804_tvf_l2d',
'hyb2_onc_20190308_032012_tvf_l2d',
'hyb2_onc_20190308_032220_tvf_l2d',
'hyb2_onc_20190308_032448_tvf_l2d',
```

```
 87  'hyb2_onc_20190308_032604_tvf_l2d',
 88  'hyb2_onc_20190308_032829_tvf_l2d',
 89  'hyb2_onc_20190308_033010_tvf_l2d',
 90  'hyb2_onc_20190308_033650_tvf_l2d',
 91  'hyb2_onc_20190308_033701_twf_l2d',
 92  'hyb2_onc_20190516_011850_tvf_l2d',
 93  'hyb2_onc_20190516_012026_tuf_l2d',
 94  'hyb2_onc_20190516_015610_tvf_l2d',
 95  'hyb2_onc_20190516_015746_tuf_l2d',
 96  'hyb2_onc_20190516_021106_tvf_l2d',
 97  'hyb2_onc_20190516_021222_tbf_l2d',
 98  'hyb2_onc_20190516_021938_tvf_l2d',
 99  'hyb2_onc_20190516_022010_txf_l2d',
100  'hyb2_onc_20190516_022114_tuf_l2d',
101  'hyb2_onc_20190516_022322_tvf_l2d',
102  'hyb2_onc_20190530_004754_tvf_l2d',
103  'hyb2_onc_20190530_012722_tvf_l2d',
104  'hyb2_onc_20190530_012858_tuf_l2d',
105  'hyb2_onc_20190530_014218_tvf_l2d',
106  'hyb2_onc_20190530_014335_tbf_l2d',
107  'hyb2_onc_20190530_015434_tvf_l2d',
108  'hyb2_onc_20190530_015642_tvf_l2d',
109  'hyb2_onc_20190530_015850_tvf_l2d',
110  'hyb2_onc_20190530_020058_tvf_l2d',
111  'hyb2_onc_20190530_022626_tvf_l2d',
112  'hyb2_onc_20190530_023543_tvf_l2d',
113  'hyb2_onc_20190530_023555_twf_l2d',
114  'hyb2_onc_20190530_023606_txf_l2d',
115  'hyb2_onc_20190530_023623_tpf_l2d',
116  'hyb2_onc_20190530_023635_tbf_l2d',
117  'hyb2_onc_20190530_023646_tuf_l2d',
118  'hyb2_onc_20190530_023724_tvf_l2d',
119  'hyb2_onc_20190530_023735_twf_l2d',
120  'hyb2_onc_20190530_023746_txf_l2d',
121  'hyb2_onc_20190530_023804_tpf_l2d',
122  'hyb2_onc_20190530_023815_tbf_l2d',
123  'hyb2_onc_20190530_023826_tuf_l2d',
124  'hyb2_onc_20190530_023904_tvf_l2d',
125  'hyb2_onc_20190530_023915_twf_l2d',
126  'hyb2_onc_20190530_023927_txf_l2d',
127  'hyb2_onc_20190530_023944_tpf_l2d',
128  'hyb2_onc_20190530_023956_tbf_l2d',
129  'hyb2_onc_20190530_024007_tuf_l2d',
130  'hyb2_onc_20190530_024405_tvf_l2d',
131  'hyb2_onc_20190530_024416_twf_l2d',
132  'hyb2_onc_20190530_024427_txf_l2d',
133  'hyb2_onc_20190530_024445_tpf_l2d',
134  'hyb2_onc_20190530_024456_tbf_l2d',
135  'hyb2_onc_20190530_024507_tuf_l2d',
```

```
136 'hyb2_onc_20190530_024618_tvf_l2d',
137 'hyb2_onc_20190530_024631_twf_l2d',
138 'hyb2_onc_20190530_024650_txf_l2d',
139 'hyb2_onc_20190530_024703_tnf_l2d',
140 'hyb2_onc_20190530_024722_tpf_l2d',
141 'hyb2_onc_20190530_024735_tbf_l2d',
142 'hyb2_onc_20190530_024754_tuf_l2d',
143 'hyb2_onc_20190613_002323_tuf_l2d',
144 'hyb2_onc_20190613_010043_tvf_l2d',
145 'hyb2_onc_20190613_010219_tuf_l2d',
146 'hyb2_onc_20190613_011539_tvf_l2d',
147 'hyb2_onc_20190613_011715_tuf_l2d',
148 'hyb2_onc_20190613_012411_tvf_l2d',
149 'hyb2_onc_20190613_012423_twf_l2d',
150 'hyb2_onc_20190613_012547_tuf_l2d',
151 'hyb2_onc_20190613_012755_tvf_l2d',
152 'hyb2_onc_20190613_013003_tvf_l2d',
153 'hyb2_onc_20190613_013211_tvf_l2d',
154 'hyb2_onc_20190613_013419_tvf_l2d',
155 'hyb2_onc_20190613_015845_tvf_l2d',
156 'hyb2_onc_20190613_015928_tvf_l2d',
157 'hyb2_onc_20190613_020045_tvf_l2d',
158 'hyb2_onc_20190613_020156_tvf_l2d',
159 'hyb2_onc_20190613_020203_tvf_l2d',
160 'hyb2_onc_20190613_020210_tvf_l2d',
161 'hyb2_onc_20190613_020217_tvf_l2d',
162 'hyb2_onc_20190613_020224_tvf_l2d',
163 'hyb2_onc_20190613_020235_twf_l2d',
164 'hyb2_onc_20190613_020247_txf_l2d',
165 'hyb2_onc_20190613_020304_tpf_l2d',
166 'hyb2_onc_20190613_020315_tbf_l2d',
167 'hyb2_onc_20190613_020327_tuf_l2d',
168 'hyb2_onc_20190613_020404_tvf_l2d',
169 'hyb2_onc_20190613_020415_twf_l2d',
170 'hyb2_onc_20190613_020427_txf_l2d',
171 'hyb2_onc_20190613_020445_tpf_l2d',
172 'hyb2_onc_20190613_020456_tbf_l2d',
173 'hyb2_onc_20190613_020507_tuf_l2d',
174 'hyb2_onc_20190613_020545_tvf_l2d',
175 'hyb2_onc_20190613_020556_twf_l2d',
176 'hyb2_onc_20190613_020608_txf_l2d',
177 'hyb2_onc_20190613_020625_tpf_l2d',
178 'hyb2_onc_20190613_020636_tbf_l2d',
179 'hyb2_onc_20190613_020648_tuf_l2d',
180 'hyb2_onc_20190613_020815_tvf_l2d',
181 'hyb2_onc_20190613_020826_twf_l2d',
182 'hyb2_onc_20190613_020838_txf_l2d',
183 'hyb2_onc_20190613_020856_tpf_l2d',
184 'hyb2_onc_20190613_020907_tbf_l2d',
```

```
185 'hyb2_onc_20190613_020918_tuf_l2d',
186 'hyb2_onc_20190613_021659_tvf_l2d',
187 'hyb2_onc_20190613_021835_tuf_l2d',
188 'hyb2_onc_20190710_232532_tvf_l2d',
189 'hyb2_onc_20190711_000721_twf_l2d',
190 'hyb2_onc_20190711_000844_tuf_l2d',
191 'hyb2_onc_20190711_002204_tvf_l2d',
192 'hyb2_onc_20190711_002321_tbf_l2d',
193 'hyb2_onc_20190711_003036_tvf_l2d',
194 'hyb2_onc_20190711_003153_tbf_l2d',
195 'hyb2_onc_20190711_003212_tuf_l2d',
196 'hyb2_onc_20190711_003420_tvf_l2d',
197 'hyb2_onc_20190711_003628_tvf_l2d',
198 'hyb2_onc_20190711_003836_tvf_l2d',
```

Index